DOI: 10.1021/cg100209v

CRYSTAL GROWTH & DESIGN
Article
2010, Vol. 10
2713–2733

Isomorphism, Disorder, and Hydration in the Crystal Structures of Racemic and Single-Enantiomer Carvedilol Phosphate

Frederick G. Vogt,*[†] Royston C. B. Copley,[‡] Ronald L. Mueller,[†,∞] Grant P. Spoors,[†] Thomas N. Cacchio,[†] Robert A. Carlton,[†] Lee M. Katrincic,[§] James M. Kennady,[§] Simon Parsons,[‖] and Olga V. Chetina[#]

[†]Preclinical Development, GlaxoSmithKline plc., P.O. Box 1539, King of Prussia, Pennsylvania 19406, [‡]Molecular Discovery Research, GlaxoSmithKline plc., New Frontiers Science Park, Third Avenue, Harlow, Essex CM19 5AW, U.K., [§]Preclinical Development, GlaxoSmithKline plc., 5 Moore Drive, Research Triangle Park, North Carolina 27709, [‖]School of Chemistry, The University of Edinburgh, West Mains Road, Edinburgh, Scotland EH9 3JJ, U.K., and [#]Chemistry Department, University of Durham, South Road, Durham DH1 3LE, U.K.

Received February 9, 2010; Revised Manuscript Received April 8, 2010

ABSTRACT: Understanding the crystalline structure of racemic carvedilol phosphate hemihydrate presents several challenges that were overcome using a combination of single-crystal X-ray diffraction, solid-state NMR (SSNMR), and other analytical techniques. Initial attempts to obtain a crystal structure were hampered by difficulties with twinning and problematic disorder in the final refinements. Multinuclear SSNMR analysis localized the disorder to portions of the molecule near the chiral center. As a result, single-enantiomer carvedilol phosphate was prepared and was found to crystallize in a phase that was isomorphous with the racemate, while SSNMR spectra of the single enantiomers did not contain the disorder observed in the racemate. The single-crystal X-ray structure of the (*R*)-enantiomer was solved and used as a starting point to successfully progress the solution of the disordered racemic crystal structure. Thermal analysis and construction of a phase diagram, along with crystallographic and spectroscopic analysis, found the crystal structure of the racemate to be a solid solution of (*R*)- and (*S*)-enantiomers, with the conformation of the molecule adjusting to fit. The crystal structures show the stoichiometry of the both the racemate and (*R*)-enantiomer to be a hemihydrate. The phase isomorphically dehydrates below relative humidity values of 1% and above temperatures of 125 °C as assessed by water vapor sorption studies, powder X-ray diffraction, and SSNMR. Single-crystal diffraction detected significant changes in the unit cell dimensions as the phase dehydrated, which was related to the visual appearance of opacity in a single crystal of the (*R*)-enantiomer. The mechanism of water incorporation was further probed spectroscopically via exchange with deuterium, ^{17}O-, and ^{18}O-labeled water; the results suggest that dehydration and rehydration likely proceed via narrow tunnels in the crystal structure, combined with the formation of fissures in the crystal. ^2H SSNMR experiments showed that the water does not engage in solid-state jump motion even at higher temperatures.

Introduction

The development of a pharmaceutical as an oral dosage form requires control over solid-state properties, in particular, the solid phase of the active ingredient, including its salt, polymorph, and solvation state.[1,2] The solid phases present in a dosage form or produced by a manufacturing process can be a critical attribute if they affect dissolution and bioavailability, product stability and shelf life, and manufacturing performance.[3] Most of the chiral pharmaceuticals currently in development are progressed as single enantiomers or single diastereomers. However, in the case of racemic mixtures of enantiomers, the two enantiomers have several options and can, for example, crystallize either as conglomerates, in which domains of a particular isomer crystallize separately, or as a crystalline racemate containing both enantiomers in close proximity in the unit cell.[4] The solid form of a racemic drug molecule may be further complicated by the existence of hydrates, a common occurrence in organic molecular solids.[5] Like nonsolvated forms, hydrates can be polymorphic and exist in forms with different molecular conformations, packing motifs, and supramolecular interactions. Hydrates may potentially occur in different states showing a well-defined stoichiometric relationship between the water and the parent molecule, while in other cases, the water content of some solid hydrates can be varied as a nonstoichiometric fraction by changing the surrounding humidity and temperature.[6−10] Unlike the usually stoichiometric isolated site hydrates, non-stoichiometric hydrates usually contain stacks or chains of water molecules in the crystal structure, and solvation and desolvation processes occur readily with little or no change to the crystal structure. The water channels can fill up to reach a maximum stoichiometry, or the crystal structure can expand to accommodate more water.[5] Various designations have been given to these types of systems: the basic labels of "variable", "non-stoichiometric", "tunnel", or "channel" hydrates, the more exact terms of "isomorphic solvate" (or desolvate),[6] or the simple addition of "$\cdot xH_2O$" to the end of a molecular formula. In the characterization of racemic and single enantiomer structures as well as isomorphic desolvation, tools such as single-crystal X-ray diffraction (SCXRD), powder X-ray diffraction (PXRD), solid-state NMR (SSNMR), and gravimetric vapor sorption (GVS) as well as thermal methods are invaluable to gain a structural understanding of macroscopic properties such as the nature of hydration and dehydration processes.[5−10]

In the present work, the solid-state structure of carvedilol phosphate hemihydrate is studied. The free base of racemic

---

*Corresponding author. E-mail: Fred.G.Vogt@gsk.com.

[∞] Present address: West Pharmaceutical Services, 101 Gordon Drive, Exton, PA 19341.

carvedilol exhibits β- and α_1-receptor blocking activity and antioxidant effects and is used for the treatment of high blood pressure and congestive heart failure, while its enantiomers block different receptors.[11−13] The chemical structure of the phosphate salt of carvedilol (Scheme 1), with the atomic numbering scheme used here, is shown below:

Scheme 1

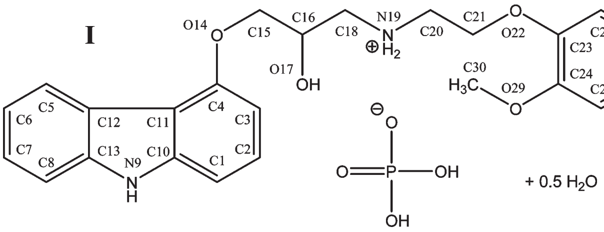
I

Carvedilol contains a chiral center (C16) and is shown as a racemate in **I**. The (*R*)- and (*S*)-enantiomers of carvedilol phosphate hemihydrate, discussed extensively in the following sections, are referred to as compounds **I-**(*R*) and **I-**(*S*). The separation of the enantiomers has been accomplished using liquid chromatography methods.[14,15]

The work described here begins with attempts to determine the crystal structure of racemic **I**, with the purpose of obtaining the structure and confirming the expected protonation state and also understanding the nature of the crystalline water. After crystallizing several forms that did not represent the bulk material, the correct solid-state form was finally obtained, but the crystal structure solution was highly complex, involving both twinning and serious disorder that was difficult to explain. Because of these challenges, a variety of additional structural studies were initiated. As part of these structural studies, the disorder was further characterized by SSNMR, which led directly to the preparation of single-enantiomer phosphate salts. These were quickly recognized as being isomorphous[16] with racemic **I** and were subsequently solved by SCXRD and were then used to rationalize and complete the structure refinement of the racemate. Thermal methods were used to study the relationship between the enantiomer structures and the racemate, leading to the finding that the (*R*)- and (*S*)-domains in the racemate were best described not as conglomerates but as a solid solution. The occurrence of solid solutions in organic molecular crystals (which are also referred to as pseudoracemates) is relatively uncommon compared to the more frequent cases of racemate structures and conglomerate formation (racemic mixtures).[17,18]

The hydration state of **I** and its enantiomers, which were found to be hemihydrates by SCXRD, was also of interest, particularly because of the unusual ability of this phase to undergo reversible isomorphic dehydration under extreme conditions. Using complementary methods, including GVS, SSNMR, Raman spectroscopy, and X-ray diffraction analyses, the water of hydration was found to be unusually tightly bound but still capable of undergoing a process similar to isomorphic desolvation. The phases can exchange a significant amount of water with surrounding atmospheric water even under ambient conditions. The evidence collected indicates that water exchange into the crystal structure is facilitated by surprisingly narrow channels and the effects of unit cell deformation.

Experimental Section

Preparation of Materials. Racemic carvedilol free base was synthesized using previously reported procedures.[19] The (*R*)- and (*S*)-enantiomers of carvedilol were resolved by preparative chiral liquid chromatography (LC) using a scaled-up version of the analytical method described below. Samples of **I**, **I-**(*R*), and **I-**(*S*) were prepared by charging a 250 mL flask with 6.2 g of carvedilol free base, 55 mL of acetone, and 1.55 mL of water. The mixture was stirred and heated to 45 °C and became clear after 10 min. The clear solution was allowed to cool to room temperature, and 1.8 g of 85% H_3PO_4 and 5.9 mL water were simultaneously added. With gentle stirring, the solution became cloudy after 15 min. After 1 h, the material was filtered, washed with acetone, and dried in an oven at 50 °C at reduced pressure (0.8 atm), for a typical yield of 95%. Various ratios of the (*R*)- and (*S*)-enantiomers were prepared as phosphate salts in a similar manner using appropriate initial ratios of the enantiomers and racemate. Grinding experiments were performed with a Restch MM200 mixer mill using 200 mg of solid powder and 3 drops of methanol. The sample was ground using a stainless steel ball at a frequency of 30 Hz for 20 min. Powders of **I** were dehydrated in a vacuum oven at temperatures of 65−70 °C. Deuterium exchange was carried out by rapidly rehydrating a vacuum-dried sample of **I** in a humidity chamber containing a saturated solution of NaCl in D_2O (Sigma-Aldrich, St. Louis, MO, USA) at 75% RH.[20] Samples that were preconditioned in a 75% RH H_2O chamber prior to deuterium exchange were also used. Analogous procedures were used to exchange ^{17}O and ^{18}O-labeled water (Cambridge Isotope Laboratories, Andover, MA, USA) into **I**.

Characterization of Purity and Structure. A chiral LC method was used to assess the enantiomeric content of the materials using an Agilent 1100 LC system (Agilent Technologies, Palo Alto, CA, USA). The chiral method used a ChiralPak AD column (250 × 4.6 mm, 5 μm particle size), an isoscratic mobile phase consisting of 82% hexanes, 12% ethanol, 6% methanol, and 0.1% trifluoroacetic acid and UV detection at 250 nm. The chemical purity of batches of **I** used in this work was confirmed to be greater than 98% w/w using an achiral LC method and an Agilent 1100 LC system. This method used a Supelco pKb-100 column (150 × 4.6 mm, 5 μm particle size), a mobile phase A with 80% water and 20% acetonitrile, a mobile phase B with 75% acetonitrile and 25% water, both with 0.05% v/v trifluoroacetic acid, a flow rate of 1.5 mL/min and UV detection at 225 nm. Mobile phase B was ramped from 2 to 7% over 10 min, then to 86% over 18 min, prior to a return to 2% for 10 min. The chemical purity of the **I-**(*R*) and **I-**(*S*) was also tested using this method, and was greater than 95%. The purity of each sample was also confirmed by ^1H solution-state NMR experiments in DMSO-d_6 solution using a Bruker DRX-700 spectrometer equipped with a broadband inverse probe. Solution-state NMR assignments were made using standard 1D and 2D NMR experiments.[21] Solution-state NMR spectra were referenced using an internal tetramethylsilane (TMS) standard for ^1H and ^{13}C experiments, an external 90% formamide standard for ^{15}N experiments, and an external 85% H_3PO_4 standard for ^{31}P experiments.[22] Optical rotation at 25 °C ($[\alpha]_D$) was measured at +7° for the (R)-enantiomer and −11° for the (*S*)-enantiomer phosphate salts using a 241 MC polarimeter (Perkin-Elmer, Waltham, MA, USA).

Solid-State NMR Spectroscopy. Solid-state NMR experiments were performed on Bruker Avance 400 and 500 spectrometers operating at a ^1H frequency of 399.87 MHz (9.4 T) and 500.13 MHz (11.7 T) respectively, equipped with variable temperature systems including a BCU-05 chiller, a liquid nitrogen heat exchanger and a liquid nitrogen boil-off gas system. Bruker MAS-II rate controllers were used to control spinning speeds to within ±2 Hz of the set point, and zirconia MAS rotors were used. ^{13}C spectra were externally referenced to TMS using hexamethylbenzene.[23] The ^{15}N spectra were externally referenced to a sample of NH_4Cl.[24] ^1H spectra were referenced by addition of a small amount of liquid TMS to the sample and repeating the analysis, while ^{31}P spectra were referenced to liquid 85% H_3PO_4 in a similar manner.[22] ^{13}C cross-polarization spectra were obtained with a Bruker 4-mm triple resonance probe tuned to ^1H, ^{13}C, and ^{15}N frequencies and spinning at an MAS rate υ_r of 8 kHz. The sample was restricted to the center of the 4-mm volume rotors to maximize RF homogeneity. A linear power ramp from 75 to 90 kHz was used on the ^1H channel to enhance CP efficiency.[25] Spinning sidebands in 1D ^{13}C spectra were eliminated by a five-pulse total sideband suppression (TOSS) sequence with a 243-step phase cycle, with a total of either 1944 or 3888 scans acquired for the spectra shown.[26] Proton decoupling was performed at an RF power of 105 kHz using the SPINAL-64 pulse sequence.[27] Edited ^{13}C spectra containing only quaternary aromatic signals were obtained using dipolar dephasing (also known as nonquaternary suppression or interrupted decoupling) during the TOSS period and three additional rotor periods using a shifted echo pulse sequence.[28] 1D ^{15}N NMR spectra were obtained with a Bruker 7-mm double resonance probe using the basic CP-MAS pulse sequence with a 5-ms contact time and a 10-s relaxation delay, and using a ^{1}H decoupling power level of ~65 kHz. A total of 4096 transients were averaged for the ^{15}N spectra. Single-pulse ^{1}H experiments were performed using a Bruker 2.5-mm double-resonance probe tuned to ^{1}H and ^{31}P frequencies and spinning at υ_r = 35 kHz. A 2.5-μs excitation pulse and a 30-s relaxation delay were used and a total of 32 transients were acquired. ^{31}P MAS and CP-MAS spectra were acquired on the 2.5 mm probe using a 2.5-μs excitation pulse and a 2 ms contact time, respectively. 2D rotor-synchronized ^{1}H double-quantum broadband back-to-back (DQ-BABA) MAS experiments were performed with 2.5-mm probes at υ_r = 35 kHz using two rotor periods of double-quantum excitation and two rotor periods of reconversion.[29] A double-quantum POST-C7 experiment was performed using ^{31}P RF field strengths of 70 kHz with υ_r = 14 kHz and a CP preparation period.[30] 2D CP heteronuclear correlation (CP-HETCOR) and heteronuclear multiple quantum coherence based on J-coupling (MAS-J-HMQC) experiments between ^{1}H and ^{13}C or ^{31}P nuclei made use of frequency-switched Lee−Goldburg (FSLG) homonuclear decoupling at 100−105 kHz with υ_r ranging from 12.5 to 15 kHz.[31,32] ^{1}H T_1 measurements were performed using saturation recovery sequences with a 100-pulse saturation comb via both direct ^{1}H observation and indirect ^{13}C detection.[33] The sample chamber temperature for MAS experiments was maintained at 273 K using a chiller except where otherwise noted, to minimize the effects of frictional heating. Static ^{2}H NMR spectra were obtained at 9.4 T with a Bruker wide-line probe using a quadrupolar echo pulse sequence.[34] The samples were loaded into the center of 5-mm glass tubes using Teflon spacers and caps. Static ^{17}O NMR spectra were obtained using a spin echo sequence at 11.7 T using a Bruker wide-line probe and a similar experimental arrangement.

X-ray Diffraction. Single crystals of **I**-(*R*) and **I** were prepared by seeding saturated solutions of the compounds in aqueous THF and aqueous methanol, respectively. The crystal and molecular structures were determined from three-dimensional X-ray diffraction data. Crystals were flash frozen and held at the data collection temperature of 90(2) K using an Oxford Cryosystems 600 Series Cryostream. All diffraction measurements were made using a Bruker-AXS SMART 6000 diffractometer with graphite monochromated Cu−Kα radiation (λ = 1.54178 Å) from a normal focus sealed tube source. The instrument was controlled using the SMART software (V5.632). The distance between the crystal and the detector was 5.0 cm. Frames were collected with the detector set in two positions (2θ = −40.00° and −108.00°). The low angle exposure times were 6 and 12 s for **I**-(*R*) and **I** respectively and 24 s for the high 2θ detector position in both cases. Each frame covered 0.20° in ω. Data integrations were carried out using the SAINT program (V6.45A), with refining box sizes. For the twinned crystal of **I**, two orientation matrices were used, with common unit cell dimensions for both domains. The twin law relating the orientations of the two domains was readily obtained from the integration software. The final unit cell parameters were taken from the integration output. A Gaussian face-indexed absorption correction was applied to the data from **I**-(*R*) using the SHELXTL program (V5.12). The data were also subsequently scaled using the SADABS program (V2.1). The absorption correction for **I** was carried out using the TWINABS program (V1.05).

The structures of **I**-(*R*) and **I** were solved by direct methods and refined by full-matrix least-squares procedures that minimized the function $\Sigma w(F_o{}^2 - F_c{}^2)^2$ using the Bruker-AXS SHELXTL software package (V6.12). For both structures, the coordinates of ordered non-hydrogen atoms were freely refined, using anisotropic atomic displacement parameters. The **I**-(*R*) structure has two molecules in the asymmetric unit (Z' = 2), as discussed in detail below, and the numbering scheme was expanded accordingly beyond that shown in Scheme 1. Atoms C51 to C68 in one of the two molecules in the asymmetric unit were disordered over two orientations, with refined complementary site occupancy factors. The atomic coordinates were refined with restraints to maintain essentially common bond lengths and angles. The atoms of the major component were refined anisotropically, while the minor component employed refined isotropic terms. In the structure of **I**, with Z' = 1, atoms C1 to C18 were disordered over three orientations with refined site occupancy factors. Geometric restraints were applied to ensure a chemically sensible and comparable result for each component. An isotropic parameter was refined as a free-variable for the non-hydrogen atoms in each component. For both structures, hydrogen atoms were generally included in calculated positions, with riding coordinates and an isotropic displacement parameter as a multiple of that of the bonded non-hydrogen atom. Hydrogen atoms bonded to nitrogen and oxygen atoms in the ordered parts of each structure had their positions refined with suitable distance restraints and employed an isotropic atomic displacement parameter. No hydrogen atom could be located for the hydroxyl group in the various disordered components found in **I**. Additional information on the single crystal diffraction studies may be found in the crystallographic information files deposited with the Cambridge Structural Database (CSD).[35]

The dehydration and rehydration studies on **I**-(*R*) were performed in situ on the SMART 6000 diffractometer using the same crystal as used for the structure analysis. Dehydration was carried out at 295 K using the nitrogen stream, which is near a 0% RH environment. Rehydration was achieved by redirecting the flow of the nitrogen stream, exposing the crystal to the ambient laboratory conditions of 24 °C ± 3 °C and 40% ± 10% RH while inside the diffractometer enclosure. The time-lapse footage was generated using the Microsoft Windows Movie Maker program (V5.1, Windows XP) from images taken with the diffractometer microscope. The time between images was calculated and incorporated into the movie, with 1 s in the movie representing 1 min in real time (see Supporting Information).

PXRD patterns were obtained under ambient conditions using X'Pert Pro diffractometers equipped with X'Celerator Real Time Multi-Strip (RTMS) detectors (PANalytical B. V., Almelo, The Netherlands). For flat-plate reflection PXRD analysis, samples were flattened onto a zero-background silicon holder and run immediately after preparation. A continuous 2θ scan range of 2° to 70° was used with a Cu−Kα (1.5418 Å) radiation source and a generator voltage of 45 kV and current of 40 mA. A step size of 0.0084° 2θ was used and individual patterns required 30 min to obtain. The goniometer radius was 240 mm. Soller slits (incident and diffracted) were set to 0.01 radians and the divergence slit (incident) and antiscatter slits (incident and diffracted) were set to 1/2°. Flat-plate reflection samples were rotated at 25 rpm. Capillary PXRD patterns were also collected under ambient conditions using an X'Pert Pro diffractometer equipped with an incident beam elliptical focusing mirror and X'Celerator RTMS detector with the same conditions as above, except for the following changes. The powder sample was filled into a 0.7-mm borosilicate glass capillary. Soller slits (incident and diffracted) were set to 0.02 radians. An effective scan rate of 0.0625° 2θ per min was used. The capillary spinner was rotated at 300 rpm. Variable humidity (VH) and variable temperature (VT) PXRD patterns were measured on an Advance D8 diffractometer using similar conditions (Bruker AXS, Madison, WI, USA). A stainless steel sample holder and an Anton-Paar TTK450 variable temperature/humidity stage were used. Temperature was controlled to within ±2 °C and humidity was controlled to within ±2% RH. Evaporated liquid nitrogen was used to cool the stage to < 100 K for low-temperature experiments. Samples on the Advance D8 system were not rotated and measurement of each pattern required 30 min.

PXRD data were refined and analyzed using the Pawley refinement procedures in the Materials Studio Reflex software package, version 4.2 (Accelrys, San Diego, CA, USA). Additional PXRD data analysis including background subtraction was performed

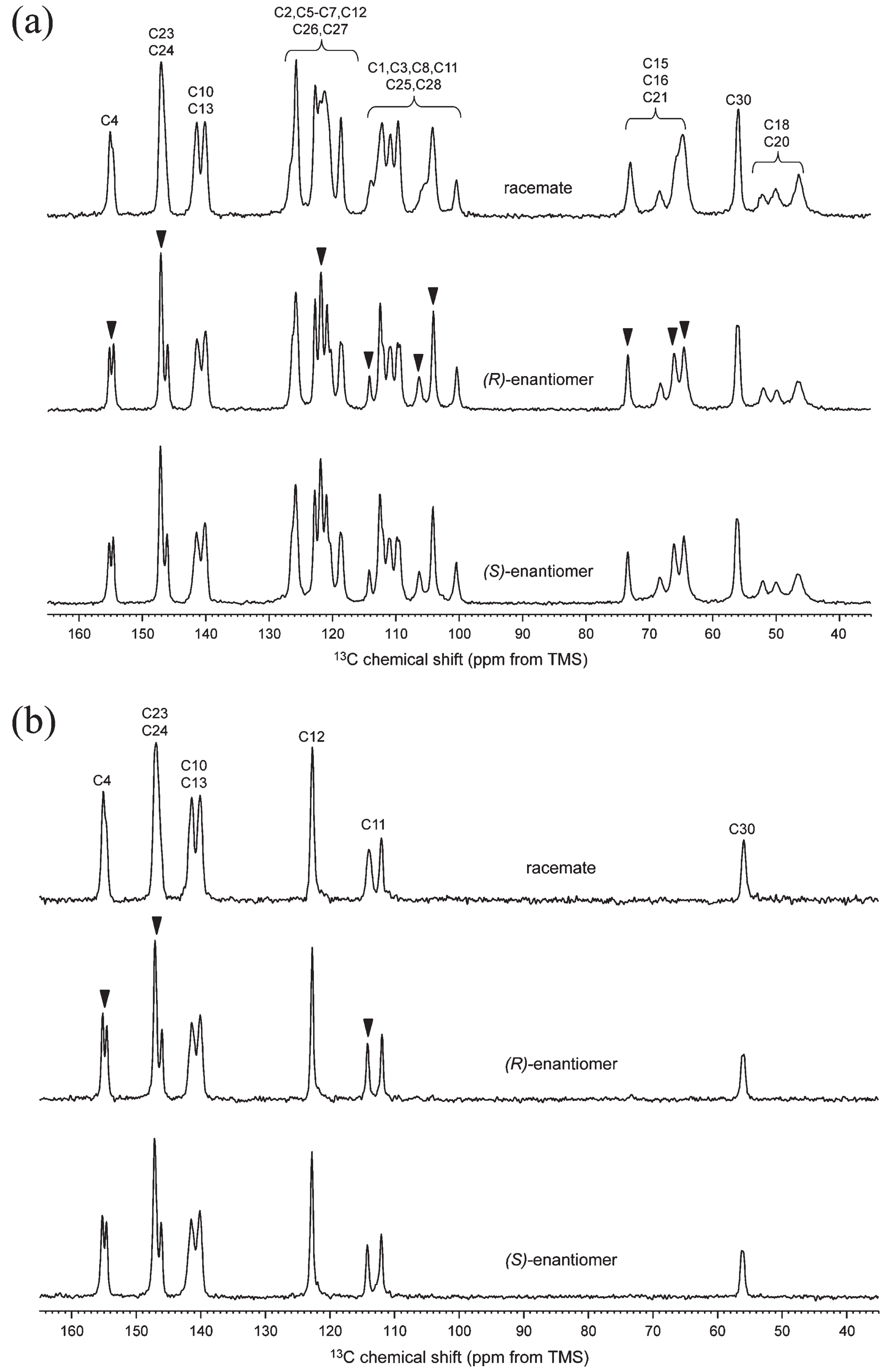

Figure 1. (a) ^{13}C CP-TOSS spectra (υ_r = 8 kHz) of **I**, **I**-(*R*), and **I**-(*S*), obtained at 273 K and 9.4 T. (b) ^{13}C CP-TOSS spectra of the same samples obtained under the same conditions but with dipolar dephasing. Key features in the enantiomer spectra (denoted with arrows) are indicative of disorder in the isomorphous racemate as discussed in the text.

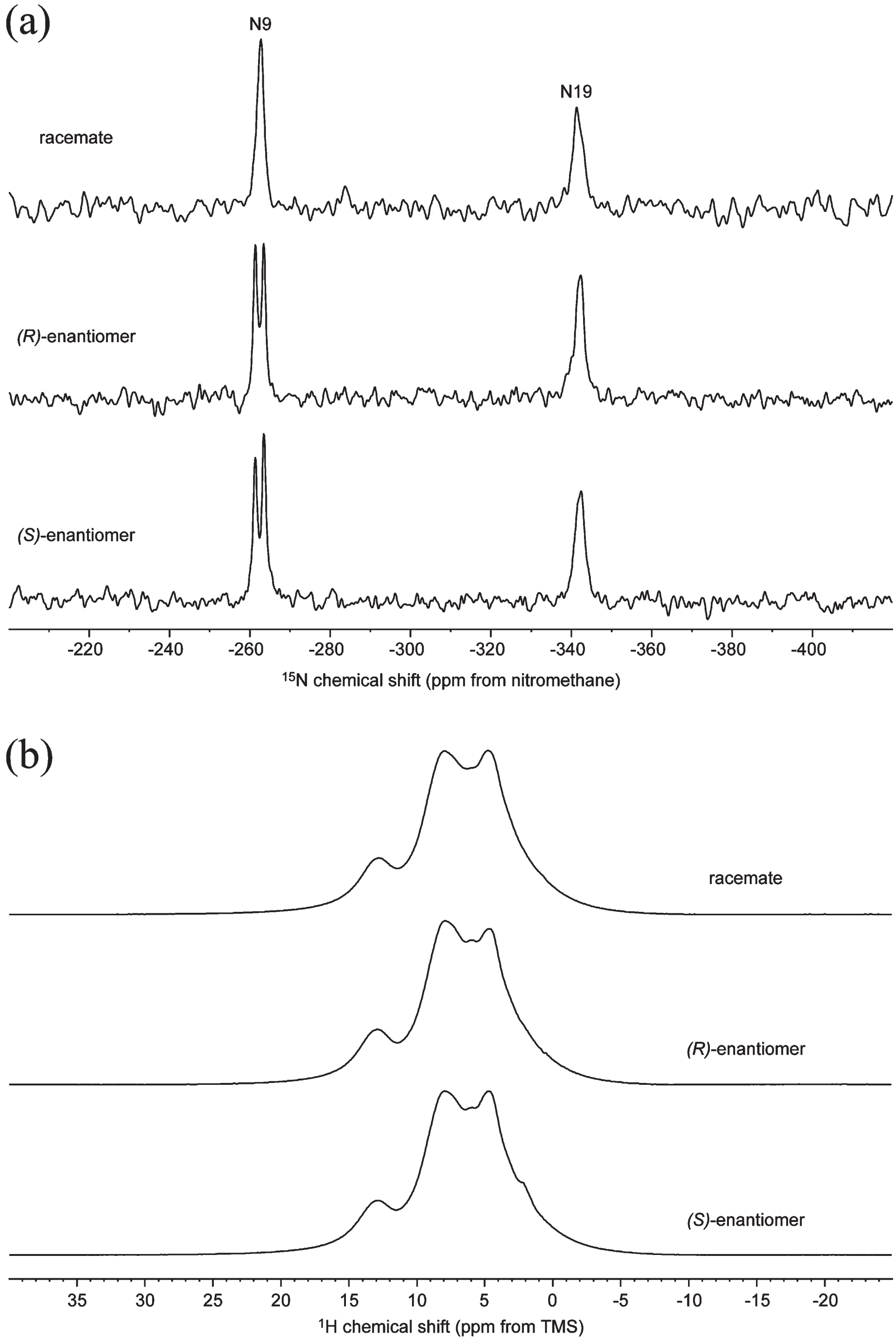

Figure 2. (a) ^{15}N CP-MAS spectra (υ_r = 5 kHz) of samples of **I**, **I**-(*R*), and **I**-(*S*) obtained at 273 K and 9.4 T. (b) ^{1}H MAS spectra (υ_r = 35 kHz) of the same samples under the same conditions.

using the HighScore Plus software package, version 2.1 (PANalytical B. V., Almelo, The Netherlands).

Vibrational Spectroscopy. Raman spectra were obtained with a Thermo Nicolet FT-Raman 960 spectrometer equipped with a Nd:YAG near-infrared laser (1064 nm wavelength), an InGaAs detector, and a CaF_2 beamsplitter (ThermoFisher, Madison, WI, USA). The laser power was 500 mW. Samples were analyzed directly in their glass vials, which were sealed immediately upon their removal from either humidity chambers or the drying oven. A total of 256 scans were averaged at a resolution of 2 cm^{-1} for each of the Raman spectra (requiring approximately 16 min). Laser-induced sample decomposition and fluorescence were not observed.

Infrared spectra were obtained using a Perkin-Elmer Spectrum One spectrometer equipped with a DTGS (deuterated triglycine sulfate) detector (Perkin-Elmer, Waltham, MA, USA). A total of 32 scans were averaged at a resolution of 2 cm^{-1} for each of the spectra, requiring approximately 10 min. Spectra were obtained using a single-bounce attenuated total reflectance (ATR) accessory with a diamond window. Samples were covered with a glass slide and pressed against the window for analysis.

Other Physical Methods. GVS experiments were performed using a DVS-1000 instrument (Surface Measurement Systems, Ltd., UK). Samples were studied over a humidity range of 0% to 90% RH at 25 °C. Each humidity step was made if less than 0.0025% weight change occurred over 10 min, with a maximum hold time of 3 h. Differential scanning calorimetry (DSC) was carried out on a Q1000 system (TA Instruments, New Castle, DE, USA). A N_2 flow rate of 50 mL/min was used. Sample sizes ranged from 0.5 to 3.0 mg, and the heating rate was 10 °C/min. Samples were run in aluminum pans, and to minimize the effects of hydration prior to the

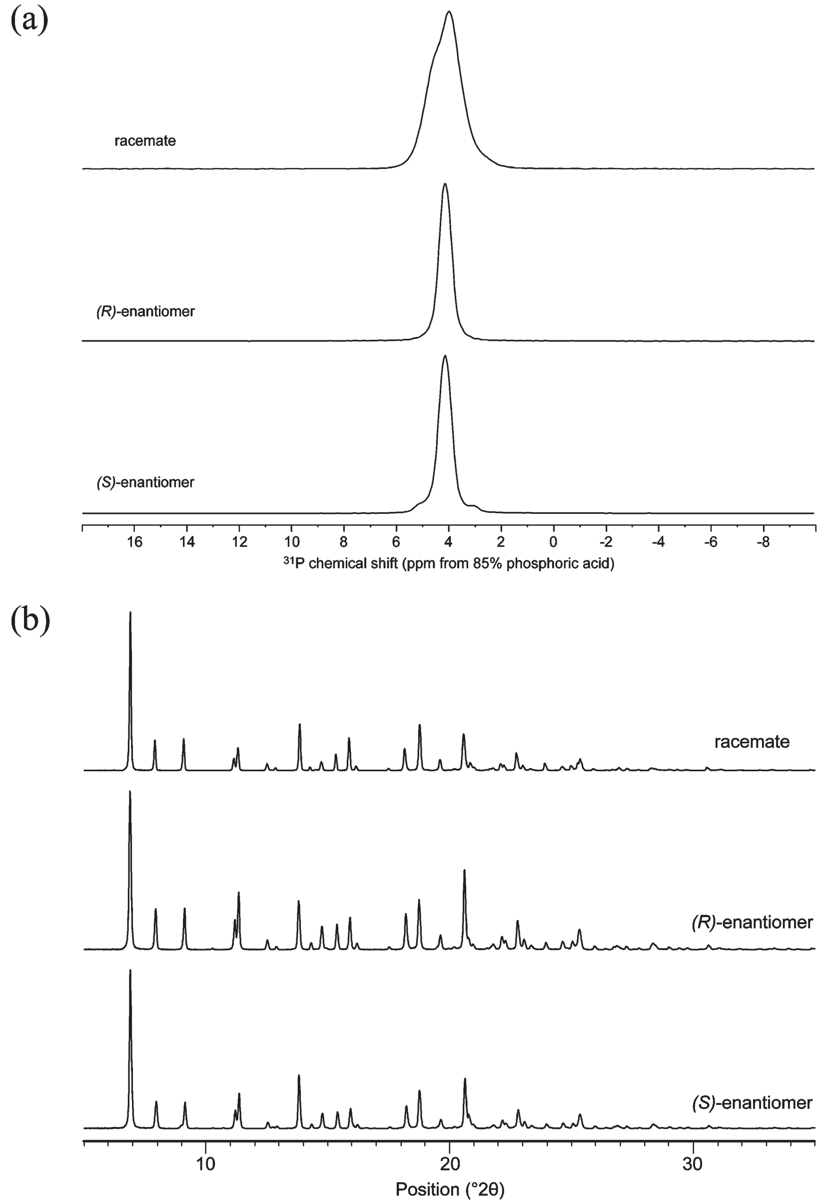

Figure 3. (a) ^{31}P CP-MAS spectra (υ_r = 25 kHz) of samples of **I**, **I**-(*R*), and **I**-(*S*) obtained at 273 K and 9.4 T. (b) Reflection PXRD patterns, measured at 298 K and ambient humidity with a flat-plate sample holder, of samples of **I**, **I**-(*R*), and **I**-(*S*).

experiment, the DSC sample was stored in its aluminum pan in the 75% RH chamber for the six-week equilibration period. As soon as the chamber was opened, a lid was pressed on the pan and the sample was analyzed. Thermogravimetric analysis (TGA) was also performed on the samples using a TA Instruments Q500 system, again using a 10 °C/min heating rate. TGA sample sizes were in the range of 5–20 mg. Coulometric Karl Fischer (KF) titrations were performed at room temperature using a Metrohm 756 KF titrator and Hydranal Coulmat reagent (Reidel-deHaan). The analysis was started within a minute of opening each vial. The system was checked before and after the analysis using a Hydranal 0.101% suitability sample traceable to NIST SRM 2890. All reported results were the average of two titrations. Surface area measurements using the Brunauer–Emmett–Teller adsorption method with nitrogen gas were performed with a Tristar instrument (Micromeritics, Norcross, GA, USA), using the average of six experiments.

Results and Discussion

Initial Solid-State NMR and PXRD Studies. Determination of the crystal structure of **I** was the initial goal of this study and was chronologically the first work attempted. Because of the complex disorder and twinning found for **I**, this structure determination presented a significant challenge and could not initially be completed. SSNMR methods were applied in an attempt to support the crystal structure analysis and learn the nature of the disorder; from this work came the valuable observation of unusual disorder in the racemate structure, suggesting further exploration of the single enantiomers. To illustrate this finding, the ^{13}C CP-TOSS spectra of **I**, **I**-(*R*) and **I**-(*S*) are shown in Figure 1a. Spectral assignments have been made using the solution-state NMR assignments given in the Supporting Information as a starting point, with more detailed assignments made using the dipolar-dephased spectra in Figure 1b and ^{1}H–^{13}C CP-HETCOR data (discussed below). The spectra shown in Figure 1 immediately suggest that the crystal structure of the racemate is isomorphous with that of the single enantiomers but contains additional disorder manifested by peak broadening (denoted by arrows in the figure). The ^{13}C assignments indicate that the disorder is present in the vicinity of a number of positions, most notably C4 and C11. Since many of these positions were near to the chiral center in carvedilol, it was hypothesized that the removal of the disorder contribution from the racemic chiral center might enable a better SCXRD result. Furthermore, the dipolar-dephased spectrum indicated that either the number of molecules in the asymmetric unit (Z') was greater than 1, or that disorder was resulting in multiple carbon environments because of the clear assignment of C4 and C11. Up until this point, attempts at structural solutions on the twinned racemate crystal had centered on $Z' = 1$ structures with significant disorder.

Additional comparisons of the **I**, **I**-(*R*), and **I**-(*S*) samples were made using other relevant NMR-active nuclei. The ^{15}N CP-MAS spectra of these samples are compared in Figure 2a. Again, through their similarity, the spectra show indications of isomorphism between the structures. A significant splitting observed for the N9 position in the enantiomers is obscured in the spectrum of the racemate, suggesting disorder involving this position. ^{1}H spectra of these samples, compared in Figure 2b, show the expected similarity but do not offer any further insight into the disorder, as the resolution of the ^{1}H spectra even at $\upsilon_r = 35$ kHz is insufficient to elucidate these effects. However, a deshielded signal at 13.0 ppm is clearly observed, which is useful for confirming structural features and will be further discussed below. The ^{31}P CP-MAS spectra of the **I**, **I**-(*R*), and **I**-(*S*) samples, shown in Figure 3a, indicate that the disorder reaches the phosphate counterion in the structure. The sample of **I** was analyzed using a ^{13}C-detected ^{1}H saturation-recovery T_1 experiment to ensure all peaks had the same ^{1}H T_1 value within the error of the experiment; a uniform ^{1}H T_1 of 7.5 ± 0.2 s was observed across the spectrum, offering no evidence of phase separation.[33] The PXRD patterns of the three materials, in Figure 3b, show no detectable difference except for minor intensity variations caused by preferred orientation. The combined data from multiple NMR spectra and PXRD thus indicate that the **I**, **I**-(*R*), and **I**-(*S*) crystal structures are isomorphous with one another, with the structure of **I** containing disorder elements near the chiral center and phosphate group but also extending throughout the molecule. Single crystals of **I**-(*R*) were then grown and analyzed by SCXRD, as discussed in the next section. Further SSNMR analysis of the detailed structural features of **I** is revisited in a later section.

SCXRD Analysis of the (*R*)-Enantiomer. A crystal of **I**-(*R*) that was a colorless plate with dimensions of 0.28 × 0.28 × 0.12 mm was successfully studied, and the asymmetric unit was found to contain two cations and two dihydrogen phosphate anions, together with half of two water molecules. The half occupancy results from the water molecules being positioned on crystallographic 2-fold axes and consequently being shared between two asymmetric units. In the remainder of this paper, the two independent cations, anions, and water molecules will be referred to as **A** and **B**, as shown in Figure 4a,b. An expanded numbering scheme beyond that given in Scheme 1 is used for the second molecule in the asymmetric unit of this $Z' = 2$ structure, as shown in Figure 4b. The diffraction study allowed the unambiguous assignment of absolute stereochemistry. The chiral centers in both independent cations were found to have the (*R*)-configuration. The final R_1 for the **I**-(*R*) structure was 3.53% and a summary of the study is presented in Table 1.

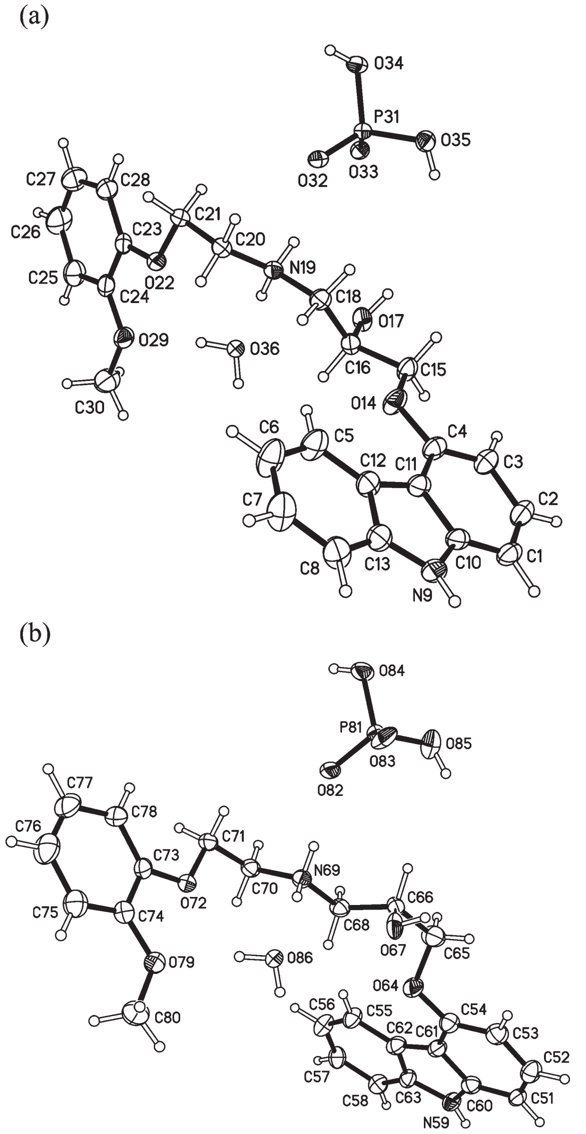

Figure 4. (a) A view of a cation **A**, anion **A**, and water molecule **A** from the single enantiomer crystal structure of **I**-(*R*). (b) A view of a cation **B**, anion **B**, and water molecule **B** from the same structure, showing only the major component of the disorder for cation **B** and showing the expanded numbering scheme. Anisotropic atomic displacement ellipsoids for the non-hydrogen atoms are shown at the 50% probability level. Hydrogen atoms are displayed with an arbitrarily small radius. Only half of the water molecule shown is in the same asymmetric unit as the cation and anion.

Several aspects of the **I**-(*R*) crystal structure are noteworthy. The fused ring system and part of the central linker of cation **B** were modeled as being disordered over two positions as shown in Figure 5a. The site occupancy factor associated with the major component was 0.784(5). The need for a second orientation was recognized when the ordered model could not be used to explain the electron density associated with C65′. For the other disordered atoms, the minor component was initially disguised by the anisotropic atomic displacement parameters, with corresponding atoms being relatively close together. Plane normals for the fused ring systems in the major and minor components are inclined at just 7.6(3)°. The conformation of the linker in cation **A** does not match that observed for either component of the disorder in cation **B**. Nonetheless, the effect of the linker is very similar in each case, and the crystal structure can be

Table 1. Summary of the SCXRD Analysis of I and I-(*R*)

structure		racemic **I**		(*R*)-enantiomer **I**-(*R*)	
moiety formula		$[C_{24}H_{27}N_2O_4]^+(H_2O_4P)^-\cdot 0.5\ H_2O$		$[C_{24}H_{27}N_2O_4]^+(H_2O_4P)^-\cdot 0.5\ H_2O$	
empirical formula		$C_{24}H_{30}N_2O_{8.50}P$		$C_{24}H_{30}N_2O_{8.50}P$	
formula weight		513.47		513.47	
temperature (K)		90(2)		90(2)	
wavelength (Å)		1.54178		1.54178	
crystal size		0.36 × 0.32 × 0.04 mm		0.28 × 0.28 × 0.12 mm	
crystal habit		colorless plate		colorless plate	
crystal system		monoclinic		monoclinic	
space group		*C*2/*c*		*C*2	
unit cell dimensions					
a	α	26.6624(7) Å	90°	26.7679(6) Å	90°
b	*β*	12.2211(3) Å	107.6220(15)°	12.2428(3) Å	108.1488(12)°
c	*γ*	16.3184(4) Å	90°	16.2786(4) Å	90°
volume ($Å^3$)		5067.7(2)		5069.3(2)	
molecules per cell (*Z*)		8		8	
molecules in the asymmetric unit (*Z*′)		1		2	
calculated density (Mg/m^3)		1.346		1.346	
absorption coeff, μ (mm^{-1})		1.419		1.418	
F_{000}		2168		2168	
theta range (°)		3.48 to 73.14		2.86 to 73.26	
index ranges		$-32 \leq h \leq 31$		$-32 \leq h \leq 32$	
		$0 \leq k \leq 15$		$-13 \leq k \leq 14$	
		$0 \leq l \leq 19$		$-15 \leq l \leq 20$	
measured reflections		5075		24604	
independent reflections		5075		9105	
R(int)		0.0000		0.0131	
coverage of independent reflections (%)		96.4		98.0	
absorption correction		semiempirical		integration	
min/max transmission		0.9454 and 0.6291		0.8537 and 0.6852	
data/restraints/parameters		5075/188/348		9105/163/767	
goodness of fit on F^2		1.447		1.042	
final *R* indices for		$R_1 = 0.1039$		$R_1 = 0.0353$	
$I > 2\sigma(I)$ data		$wR_2 = 0.3203$		$wR_2 = 0.0960$	
final *R* indices for		$R_1 = 0.1128$		$R_1 = 0.0357$	
all data		$wR_2 = 0.3295$		$wR_2 = 0.0964$	
absolute structure parameter		not applicable		0.001(13)	
largest diff peak and hole		1.080 and −0.416 e $Å^{-3}$		0.390 and −0.226 e $Å^{-3}$	

described as pseudocentrosymmetric, with the rings of the independent cations, the anions, and the water molecules being related by approximate inversion symmetry as seen at the center of Figure 5b. This symmetry breaks down in the linker since only one enantiomer is present. The intermolecular interactions associated with the corresponding independent cations, anions, and water molecules are broadly related by the pseudoinversion symmetry. However, one important difference relates to the interactions of the hydroxyl groups in cation **A** and cation **B**. For the former, a strong and direct interaction to O33 is observed. Since the anions are related by the approximate inversion symmetry but the chiral center and the attached hydroxyl group are not, an analogous interaction is not observed for cation **B**. Instead, the hydroxyl group of both components has a longer, bifurcated interaction with O82 and O83. The lack of a more direct interaction may explain why cation **B** is disordered in this region.

The two independent anions are arranged as a dimeric unit about a pseudoinversion center, linked by the O−H···O hydrogen bonds shown in Figure 5b. The dimeric units are themselves linked by further O−H···O hydrogen bonds, generating chains of anions that run in the direction of the crystallographic *c*-axis. Within a chain, the order of the anions can be described as **AABBAABB...**, while the P31···P31, P31···P81, and P81···P81 separations are 4.0302(8), 4.2835(5), and 4.0420(8) Å, respectively. One water molecule in the **I**-(*R*) crystal structure donates a hydrogen bond to O29 [2.775(2) Å] and accepts one from N19 [2.872(2) Å] of cation **A**, with two further symmetry related interactions being generated by virtue of the 2-fold axis. With four hydrogen bonding interactions in total, the water can be thought of as being strongly bound in the structure. The significance of the strongly bound water will be discussed in conjunction with SSNMR and GVS measurements in a later section. As expected, given the pseudosymmetry, the other water molecule has an analogous environment between cation **B** and its symmetry equivalent.

In summary, the untwinned **I**-(*R*) crystal contained disorder that was easily modeled, allowing a clear indication of the atomic connectivity, chemical composition, and hydration state, all of which are of value in solving the racemate structure. The structure has $Z' = 2$, in full agreement with the splitting observed in the ^{13}C and ^{15}N SSNMR spectra for N9, C4, C11, and other positions. The strong splitting seen for the C11 position is traceable to the conformational change between cation **A** and **B** near to this atom, as seen in Figure 4. For example, the C11−C4−O14−C15 torsion angle for cation **A** is −175.54(18)°; the equivalent C61−C54−O64−C65 torsion angle for the major component of the disordered cation **B** is −129.1(3)°. The lack of a splitting in the ^{31}P spectrum and for the N19 signal in the ^{15}N spectrum is likely related to the approximate inversion symmetry found in the **I**-(*R*) structure. A PXRD pattern simulated from the crystal structure and subjected to Pawley refinement agrees with the pattern measured on powders, as shown in the Supporting Information, indicating that the crystal analyzed here was representative of bulk material.[36]

Analysis of Twinning in the SCXRD Data of Racemic I. With a full understanding of the **I**-(*R*) crystal structure, efforts were redirected toward understanding the twinned

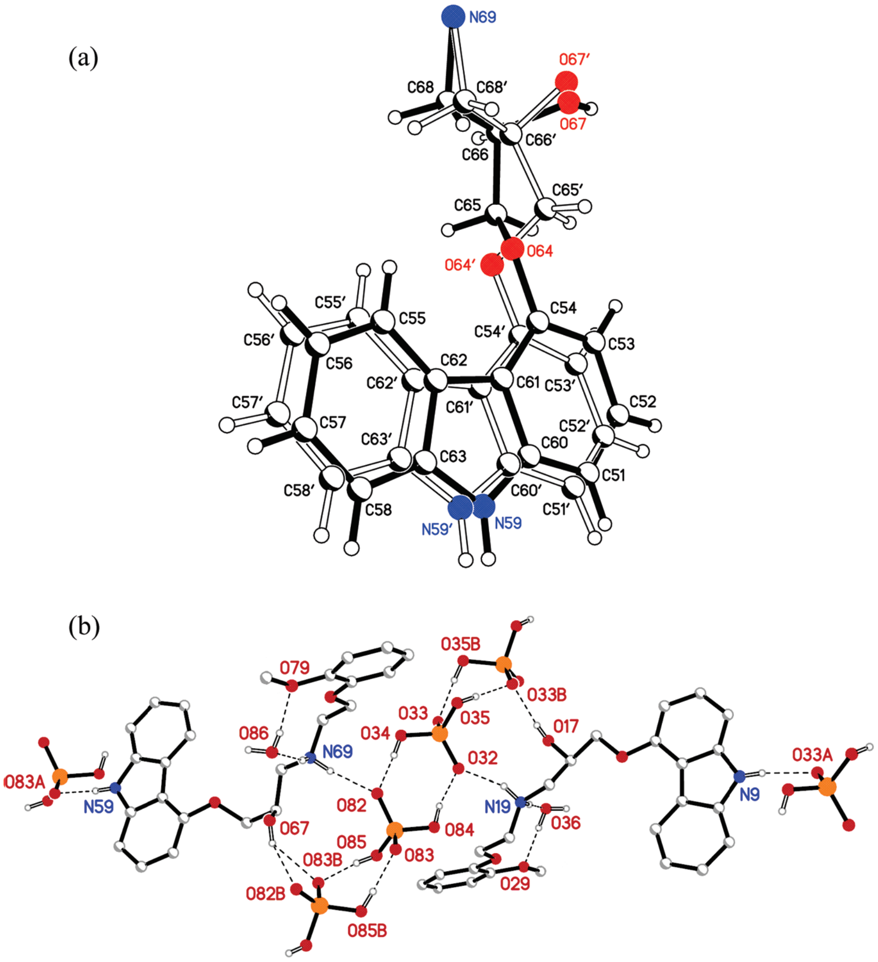

Figure 5. (a) Illustration of the two components of the cation **B** disorder in the crystal structure of **I**-(*R*). The major component is shown with a solid bond type. The ordered portion of cation **B** (apart from N69) has been omitted for clarity. (b) Hydrogen-bonding observed for the crystal structure of **I**-(*R*), highlighting the pseudocentrosymmetric packing arrangement. Hydrogen bonds are shown as dashed lines. Hydrogen atoms (except N*H* and O*H*) and the minor component of the cation **B** disorder have been omitted for clarity.

crystal of **I**. The twinning was apparent from the room temperature diffraction pattern, which was characterized by split peaks, particularly at high resolution. This pattern was indexed on the basis of two orientation matrices related by the following twin law:

$$\begin{pmatrix} 1 & 0 & 0.93 \\ 0 & -1 & 0 \\ 0 & 0 & -1 \end{pmatrix}$$

At 90 K, splitting of the peaks was not observed, and a single orientation matrix was sufficient to index all the diffraction spots. The monoclinic unit cell obtained at 90 K can be transformed to a metrically orthorhombic unit cell, with approximate dimensions of a = 16.31 Å, b = 50.79 Å, c = 12.22 Å, $\alpha = \beta = 90°$, and $\gamma = 89.96°$ using the matrix **M**:

$$\begin{pmatrix} 0 & 0 & -1 \\ -2 & 0 & -1 \\ 0 & 1 & 0 \end{pmatrix}$$

Merging the transformed data set in point group *mmm* yielded $R_{\text{int}} = 0.0829$. Merging the data as originally indexed in point group 1 1 2/*m* yielded $R_{\text{int}} = 0.0357$. The merging in 2/*m* was clearly superior, indicating that the crystal system is monoclinic. However, the merging statistics in *mmm* is only slightly worse. In neither case was the space group obvious from examination of systematic absences. Both of these features are indicative of twinning.[37]

At low temperature, derivation of the twin law can be accomplished by analysis of the unit cell dimensions.[38] Let $\boldsymbol{a}_{\mathbf{o}}$, $\boldsymbol{b}_{\mathbf{o}}$, and $\boldsymbol{c}_{\mathbf{o}}$ be the basis vectors of the orthorhombic cell, and $\boldsymbol{a}_{\mathbf{m}}$, $\boldsymbol{b}_{\mathbf{m}}$ and $\boldsymbol{c}_{\mathbf{m}}$ be the basis vectors of the monoclinic cell. Possible twin laws correspond to 2-fold rotations about $\boldsymbol{a}_{\mathbf{o}}$ or $\boldsymbol{b}_{\mathbf{o}}$ (R_{ao} and R_{bo}): $\boldsymbol{c}_{\mathbf{o}}$ need not be considered as this corresponds to $\boldsymbol{b}_{\mathbf{m}}$, where there is a 2-fold axis due to the monoclinic symmetry. The triple matrix products ($M^{-1}R_{ao}M$ and $M^{-1}R_{bo}M$) allow these 2-fold rotations to be expressed in terms of the monoclinic cell as:

$$\begin{pmatrix} -1 & 0 & -1 \\ 0 & -1 & 0 \\ 0 & 0 & 1 \end{pmatrix} \text{ and } \begin{pmatrix} 1 & 0 & 1 \\ 0 & -1 & 0 \\ 0 & 0 & -1 \end{pmatrix}$$

Note the similarity of the second of these matrices to that derived from the room-temperature data set above. The off-diagonal term ($-2a_m \cos \beta_m / c_m$) is essentially unity at 90 K (0.99 from the diffractometer integration software) but significantly nonintegral at room temperature, explaining why the diffraction spots were clearly split under ambient conditions.

SCXRD Structure of Racemic I. As with **I**-(*R*), the crystal of **I** studied was also a colorless plate (0.36 × 0.32 × 0.04 mm). The asymmetric unit was found to contain a single cation,

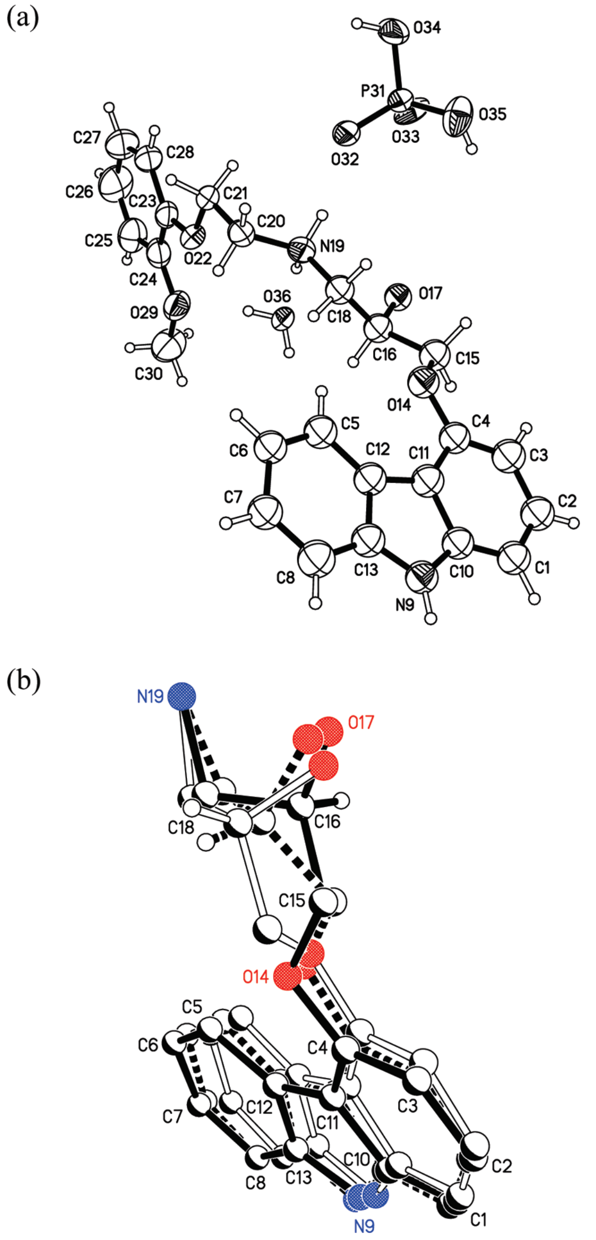

Figure 6. (a) A view of a cation, anion, and water molecule from the crystal structure of racemic **I**. Half of the water molecule shown is in the same asymmetric unit as the cation and anion. The hydrogen atom associated with O17 was not located. Only the first component of the C1−C18 disorder is shown, with these atoms being refined isotropically. Anisotropic atomic displacement ellipsoids for the remaining non-hydrogen atoms are shown at the 50% probability level and hydrogen atoms are displayed with an arbitrarily small radius. (b) The three components of the cation disorder. Each component is shown with a different bond type (**1** − solid; **2** − open; **3** − dashed). Only component **1** is labeled. Hydrogen atoms, apart from those associated with the chiral center, have been omitted, as has the ordered portion of the cation, apart from N19.

a dihydrogen phosphate anion, and half a water molecule, as shown in Figure 6a. As before, the half-occupancy of the water molecule results from it being positioned on a crystallographic 2-fold axis. The unit cell dimensions for **I**-(*R*) and **I** at 90 K are closely related and compared in Table 1. In making this comparison, it is essential to make sure that in both cases, C-centered cells are being considered. This is because the alternative I-centered cells have very similar unit cell dimensions. The **I**-(*R*) structure was described as pseudocentrosymmetric, and the structure of **I** has essentially been modeled as a true centrosymmetric variation of this. Indeed, instead of using direct methods, the structure of **I** could also be solved by simply starting from the coordinates of the ordered molecule from the **I**-(*R*) structure and applying the correct space group symmetry and origin shift.

In terms of the twinning and disorder present, the structure of **I** is far more complex than **I**-(*R*), as reflected by its relatively high R_1 value of 10.39%. In the crystal structure of **I**-(*R*), the fused ring system and part of the central linker of cation **B** were modeled as being disordered over two positions. For the crystal structure of **I**, three similar components of disorder (henceforth referred to as **1**, **2**, and **3**) had to be modeled and are depicted in Figure 6b. The site occupancy factors for the three components were 0.368(3), 0.319(7), and 0.313(8), respectively. It was not possible to locate the hydroxyl hydrogen atom for any of the cation's components. Alternative models of the disorder were also obtained during this study, including a model in which only a small subset of the atoms in the fused ring system and the central linker were modeled as being disordered. Although this approach is simpler and required fewer refinement parameters, much of the physical significance of the disorder was lost. The use of three components avoids this and also ensured that realistic chemical environments were maintained for the disordered atoms. The orientation of the fused ring system is similar in each of the three components. Considering how the plane normals for the fused rings in the components are inclined relative to one another, the largest angular deviation, between **1** and **2**, is just 7.8(5)°. An effectively identical finding was noted for cation **B** in the crystal structure of **I**-(*R*). The absolute configuration modeled for component **1** is different to that of **2** and **3**. This finding implies disorder of the two enantiomers over the cation sites. Although the model does not have an equal distribution of the two enantiomers on each site, the (*R*)- and (*S*)-cations are present in equal proportions overall. This is because an equally disordered but inverted arrangement is generated elsewhere by space group symmetry.

The largest peak in the Fourier difference map at the end of the refinement (1.08 e Å^{-3}) was believed to be associated with yet another cation component, with the peak corresponding to a new position for O14. With a much lower occupancy than the other three components, the possible new component appeared to contribute little to the overall electron density and also proved difficult to refine. As such, it was not included in the final structural model. Extensive efforts to resolve the cation disorder by changing the space group were unsuccessful. Slightly lower R_1 values could be obtained using subgroups but only at the cost of introducing additional refinement parameters. With pseudosymmetry being a large issue in these subgroups and with no clear advantage being demonstrated, the $C2/c$ space group was retained.

The phosphate anion was modeled in only one orientation. While this represents a simplification of the true arrangement given the results of the ^{31}P SSNMR experiment, efforts to refine the anion as a multicomponent system, to match the variety shown by the cation, led to complex models with few advantages. As previously reported for the structure of **I**-(*R*), the anions are arranged in chains. Within these chains there are two independent P···P separations, 4.039(2) and

4.284(2) Å, similar to the three distances found for **I**-(*R*). Despite the complexity of the racemic structure, it was possible to identify most of the hydrogen bonds and the water environment, which are closely related to that seen in **I**-(*R*). Indeed, most of the hydrogen bonds identified can be easily related to corresponding interactions for the structure of **I**-(*R*). Since the hydroxyl hydrogen atoms for the various components of the cation disorder of **I** were not located, no hydrogen bonds involving this group could be identified. However, close O···O contacts indicate possible interactions. There appears to be more than one bonding option available to these hydrogens, which, along with the packing requirements, may help to explain the disorder observed in the structure.

The SCXRD analysis indicates that the crystal structure of racemic **I** contains intimately mixed (*R*)- and (*S*)-enantiomers in which the conformation of the molecule has adjusted to fit. The significance of the interaction between the two enantiomers is discussed further in the following sections. To verify that bulk samples of **I** were representative of the crystal structure determined here, a Pawley refinement was performed against a high-resolution experimental capillary PXRD pattern of **I** and was found to be in agreement, with the results shown in the Supporting Information.

SSNMR Structural Analysis of Racemic I. The SSNMR data obtained for **I** was closely examined for effects that would confirm the SCXRD structure and disorder model. To verify that key elements of the crystal structures of **I** and **I**-(*R*) matched with available SSNMR data, additional 2D SSNMR analysis was performed. A ^{1}H DQ-BABA homonuclear correlation spectrum is shown in Figure 7a.[29] This spectrum helps facilitate comparison of ^{1}H dipolar interactions for the distinctive signal at 13.0 ppm with the SCXRD structure. The interpretation of the ^{1}H DQ-BABA data confirms three short (~2.5 Å) hydrogen−hydrogen interactions in the crystal structure of **I**, primarily involving H34 and H35 (as N9H is not involved in sufficiently short interactions). To confirm the assignment of the deshielded ^{1}H signal at 13.0 ppm to N9H, H34, and H35, two ^{1}H−^{31}P CP-HETCOR experiments[31] with mixing times of 100 and 500 μs were performed; the results obtained using the latter mixing time are shown in Figure 7b. A strong correlation is seen between P31 and the deshielded ^{1}H signal at 13 ppm; this interaction arises primarily from the short interactions with H34A and H35A of 2.0 Å. This was confirmed by comparison to the ^{1}H−^{31}P CP-HETCOR experiment performed with a 100 μs contact time (not shown); in this spectrum only the correlation between P31 and the ^{1}H signals at 13.0 ppm was detected. The assignment of the other proton signals in Figure 7b was made in conjunction with the SCXRD structure of **I** and the ^{1}H−^{13}C CP-HETCOR spectrum of **I** obtained with a 500 μs contact time (see Supporting Information).[31] No intermolecular dipolar correlations useful for confirming aspects of the crystal structure could be located in the ^{1}H−^{13}C CP-HETCOR spectrum of **I**, although the spectrum did assist with the ^{1}H and ^{13}C assignments given here including confirmation of the assignment of N9H.

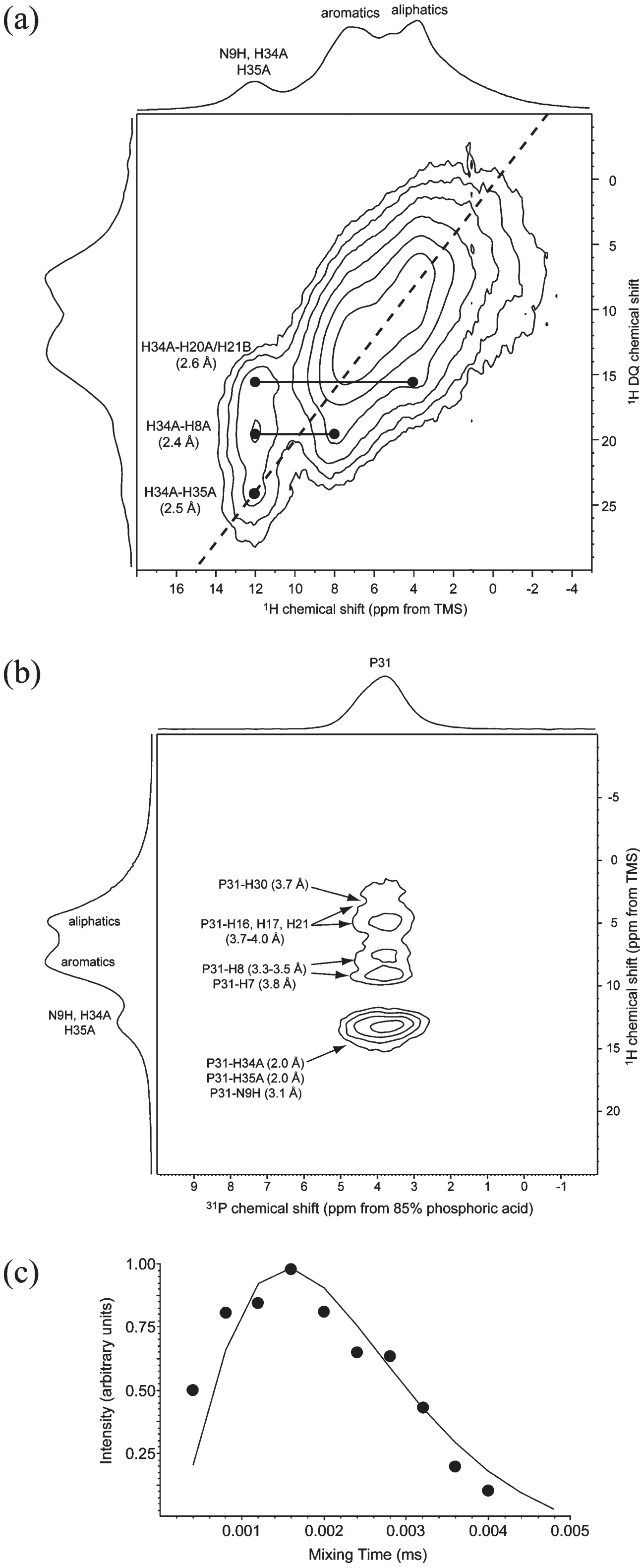

Figure 7. (a) ^{1}H DQ-BABA spectrum (υ_r = 35 kHz) of a sample of **I** obtained at 11.7 T. (b) ^{1}H−^{31}P CP-HETCOR spectrum (υ_r = 15 kHz) obtained at 9.4 T using a 500 μs contact time. (c) Build-up of DQ coherence as a function of ^{31}P DQ-POST-C7 mixing time (obtained at 9.4 T), showing experimental values (points) and a simulated line (see text). All spectra were obtained at 273 K.

The ^{1}H−^{13}C CP-HETCOR spectrum of **I**, combined with the ^{1}H−^{13}C MAS-J-HMQC spectrum (see Supporting Information) provides useful evidence of an edge-on aromatic π-stacking interactions through ^{1}H shielding effects.[39,40] One notable effect involves H3A and the ring defined by C5−C6−C7−C8−C12−C13 through a ^{1}H−^{13}C correlation at 105.5 ppm and 5.5 ppm, the latter being significantly shielded relative to the ^{1}H shift of H3 in solution (6.69 ppm), as is often observed in π-stacked aromatic organic and pharmaceutical crystals.[41−43] The distance between the centroid of this ring and H3A was 3.1 Å in the major component of the disordered structure, explaining the shielding effect on the ^{1}H shift of H3. The neighboring H2 signal, which appears at 7.29 ppm in solution, also shows a similar but less pronounced shielding trend to 6.2 ppm, as it has a greater distance to the ring centroid. Another strong edge-on aromatic π-stacking interaction is also observed through a ^{1}H−^{13}C correlation at 110.2 ppm and 4.5 ppm, which is assigned to an interaction between H25 and the ring defined by C1−C2−C3−C4−C11−C10, with a H25A-to-centroid distance of 2.7 Å (measured using the major component of the disordered model). Again, this proton signal is significantly shielded relative to its value in solution (6.96 ppm). The observation of these aromatic interactions in both the crystal structure and SSNMR data thus help confirm the crystal structure of **I**.

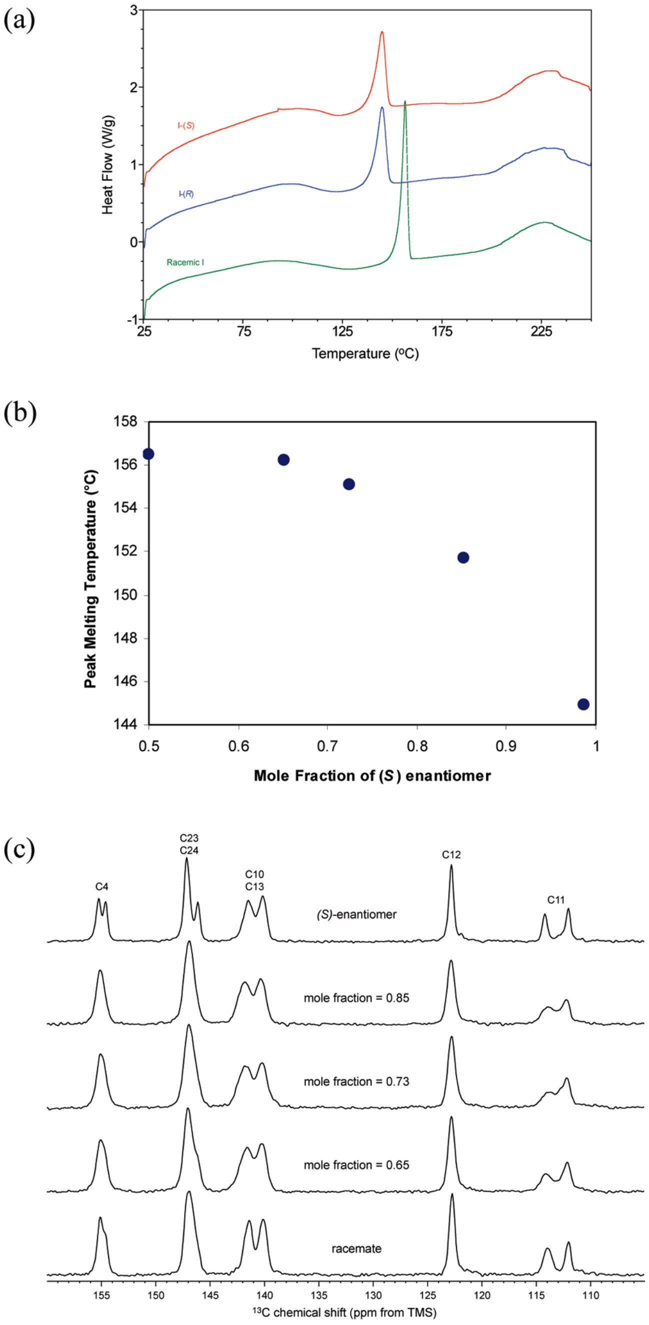

Figure 8. (a) DSC thermograms of racemic **I**, **I**-(*R*), and **I**-(*S*). Exothermic events are plotted in the downward direction. (b) Diagram constructed from samples crystallized with different enantiomeric input ratios, showing the peak temperature of the melt plotted against the mole fraction of the (*S*)-enantiomer in the solid solution as measured by chiral LC (see text). (c) Expansions of the ^{13}C dipolar-dephased spectra of the samples in (b), obtained at 273 K and 9.4 T.

To confirm that the phosphorus atoms were near in space to one another and arranged in near-linear chains as seen in the crystal structure of both **I** and **I**-(*R*), a ^{31}P DQ-POST-C7 experiment (with a ^{1}H−^{31}P preparation period and ^{1}H decoupling) was conducted on a sample of **I** during which the DQ excitation period was incremented.[30] The results of this experiment are plotted in Figure 7c, where the excitation of DQ coherence is compared to a theoretical curve simulated for a 4.0 Å $P \cdots P$ internuclear distance using an empirical expression that has been developed for phosphate networks in glasses.[44] Although a full analysis of the multispin DQ excitation behavior expected from linear chains of phosphorus atoms is beyond the scope of this work, the results shown in Figure 7c are a useful confirmation of the proximity of the phosphorus atoms in the structure of **I**.

Finally, the observation of disorder in the ^{13}C spectra also serves as a check of the crystal structure, as disordered positions in the SCXRD structure should correlate with disordered positions in the SSNMR spectra. This is the case here; for example, in Figure 1a,b, positions C4, C15, C16, and C21 (all of which are near to the chiral center) are seen to be broadened in the SSNMR spectra; these same positions are the most disordered in the final crystal structure, as was originally noted at the start of the efforts to produce the single enantiomer salts. The ^{13}C signal for C11 observed using dipolar dephasing shows the most structure, with two clearly resolved peaks, the more deshielded of which shows evidence of additional unresolved splitting. As was the case with the crystal structure of **I**-(*R*), the structure observed for the C11 position is likely related to conformational changes involving O14 and its attached chain, as seen in Figure 5b. The signal for C11 suggests at least three significant components for the disorder model, in agreement with the three-component model used here for the crystal structure of **I**. However, as it was not possible to fully resolve the three components of the disorder modeled in the crystal structure of **I** in any of the multinuclear SSNMR spectra, even at 11.7 T, no direct comparison with the relative occupancies in the SCXRD structure could be made.

Thermal Analysis. DSC studies of **I**, **I**-(*R*), **I**-(*S*), and mixtures of different mole fractions of the enantiomers were also performed to determine whether **I** crystallized as a racemic mixture (single enantiomer conglomerates) or as a solid solution containing intimately mixed (*R*)- and (*S*)- enantiomers.[17,18] The DSC traces for samples of **I**-(*R*) and **I**-(*S*) are compared with that of **I** in Figure 8a. The peak temperature of the melting endotherm for the enantiomers occurs at 144.8 and 144.9 °C for **I**-(*R*) and **I**-(*S*), respectively, compared to 156.5 °C for **I**. The broad endotherm between 60 and 125 °C for all three samples corresponds to loss of water of hydration, discussed in more detail below. Given the similar purity values determined for these materials, the melting point behavior is assigned to the formation of a solid solution of the enantiomers in **I**.[17,18] The heats of fusion for the enantiomers were 37.4 and 36.5 J/g for **I**-(*R*) and **I**-(*S*), respectively, compared to 46.9 J/g for **I**, suggesting a stabilization energy of approximately 10 J/g for **I** over its enantiomers. A series of crystallizations were carried out using mixtures of the (*S*)-enantiomer and racemic carvedilol as input material, to obtain mixtures of **I** and **I**-(*S*). The melting points of these mixtures are plotted in Figure 8b against the actual molar ratios determined by chiral LC, and match the trend expected for a solid solution.[18] The DSC results thus demonstrate that racemic **I** exists as a solid solution (also referred to as a pseudoracemate) as opposed to phase-separated conglomerates of (*R*)- and (*S*)- domains.[18] This can be anticipated given their similar unit cells and crystal structures, but as solid solutions are rarely encountered,[45−49] DSC analysis is necessary to confirm this structural feature.[18]

In Figure 8c, expanded regions of the dipolar-dephased SSNMR spectrum are shown for the crystallized samples with different molar ratios. As the excess of the (*S*)-enantiomer increases, the C4, C11, and several other positions show broadening behavior characteristic of additional disorder. This illustrates the molecular level effect of extra (*S*)-enantiomer in the intermediate mole ratio solid solutions, creating domains of the (*S*)-enantiomer and disrupting the stabilizing disorder model seen in the racemate. The full ^{13}C CP-TOSS and ^{31}P CP-MAS spectra of these samples show similar but less pronounced effects (see Supporting Information).

An equimolar sample of **I**-(*R*) and **I**-(*S*) was also produced by solvent-drop grinding (SDG) with methanol, using the same enantiomer samples that melted at ∼145 °C, in an attempt to produce a solid solution in a different manner to the direct crystallization approaches used above. The use of SDG to produce crystalline solid solutions has been previously demonstrated.[50] The DSC thermogram for this sample yielded a peak temperature of 153.8 °C and an enthalpy of fusion of 45.4 J/g for the melting endotherm; the ^{13}C SSNMR spectra of this sample showed additional broadening in the disordered regions associated with the chiral center but otherwise resembled the spectra of **I** produced by crystallization (see Supporting Information). This sample is thus likely a partially mixed solid solution, in which the enantiomers have not reached their optimal low-energy structure because of the more limited mixing process afforded by the SDG technique in comparison to solution crystallization.

The results of the DSC, SSNMR, and SCXRD studies show that the nearly isomorphous nature of the single enantiomer and racemate structures allows for formation of a solid solution. Solid solutions of organic enantiomers[45−47] and partial solid solutions[48,49] are not commonly encountered; conglomerate and racemic crystal structures are far more frequently observed.[17,18] From the crystallographic perspective, the occurrence of the solid solution can be easily rationalized, given that the *C*2/*c* space group of the crystal structure of **I** incorporates inversion centers not found in the *C*2 space group of the enantiomer; comparison of the structures suggests that the **I**-(*R*) structure would prefer to be centrosymmetric but cannot easily do so because of its uniform chirality. Additionally, the crystal structure of **I** may simply satisfy intermolecular interactions in a more energetically favorable way, thus leading to enthalpy-based stabilization of the free energy. Since the crystal structure of the solid solution of **I** shows only a slight increase in density relative to that of the **I**-(*R*) structure (systems which obey Wallach's rule usually show a more significant increase in density),[51,52] it appears that greater satisfaction of intermolecular interactions, such as van der Waals forces, drives the increase in free energy in **I** over **I**-(*R*). This argument is bolstered by the lack of any detectable peak shift changes in the deshielded region of the ^{1}H SSNMR spectra of **I** when compared to **I**-(*R*), since ^{1}H chemical shifts are sensitive to minor changes in hydrogen bond geometry.[53]

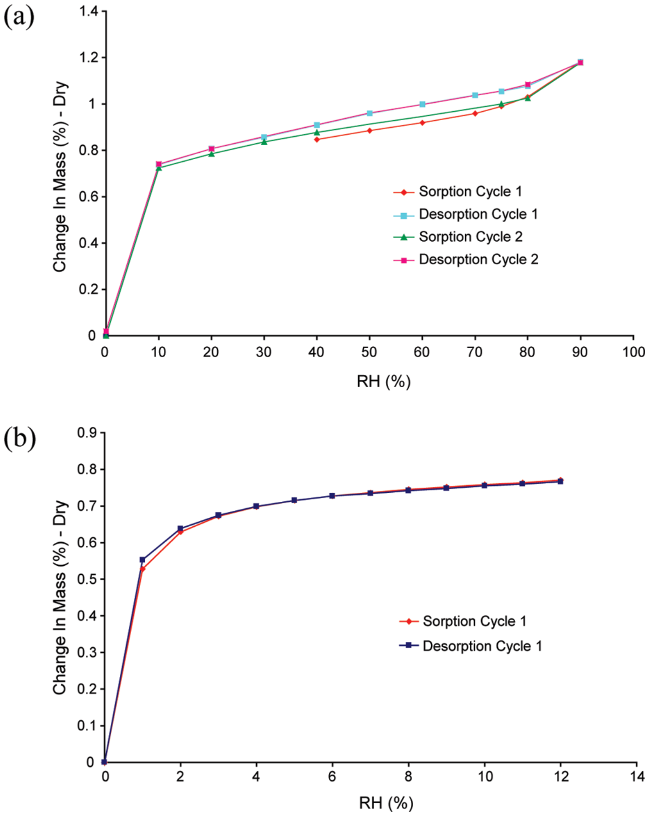

Figure 9. GVS isotherms obtained at 25 °C for a powder sample of racemic **I**. (a) Isotherm obtained with 10% RH steps from ∼0% RH (dry nitrogen) to 90% RH. (b) Isotherm obtained with 1% RH steps from ∼0% RH (dry nitrogen) to 12% RH. The water is not fully removed at the lowest RH achieved in this experiment; higher temperatures and reduced pressures are needed to remove more of the water, although the process remains fully reversible up to the melting temperature.

GVS, PXRD, and SSNMR Studies of Dehydration. The second interesting feature of the crystal structure of **I**, namely, the nature of the water in the structure, also required investigation using a multidisciplinary approach. The theoretical water level is 1.8% w/w for the hemihydrate found by SCXRD; however, the water in powder samples could be readily lowered to 1.2% w/w by vacuum drying at slightly elevated temperatures (e.g., 65 °C) and quickly analyzing samples by Karl Fischer titration (KFT). However, some rehydration likely occurred during sample weighing and transfer to the KFT titration media, so that the reported value of 1.2% w/w should be considered to be an upper limit with the actual moisture level being lower. GVS was used to assess the change in water content of **I** with humidity. The isotherm in Figure 9a, which is a typical Type I isotherm,[2,54] shows a feature at 10% relative humidity (RH) that indicates a significant change in hydration state. Steps of 10% RH were used to obtain these data. A more precise determination of the critical RH was obtained by stepping the GVS isotherm in 1% RH increments, as shown in Figure 9b; this indicates a critical RH of approximately 1% RH. Significant water loss is observed between 10% and 1% RH. Between 10% and 90% RH, the water content of **I** can reversibly

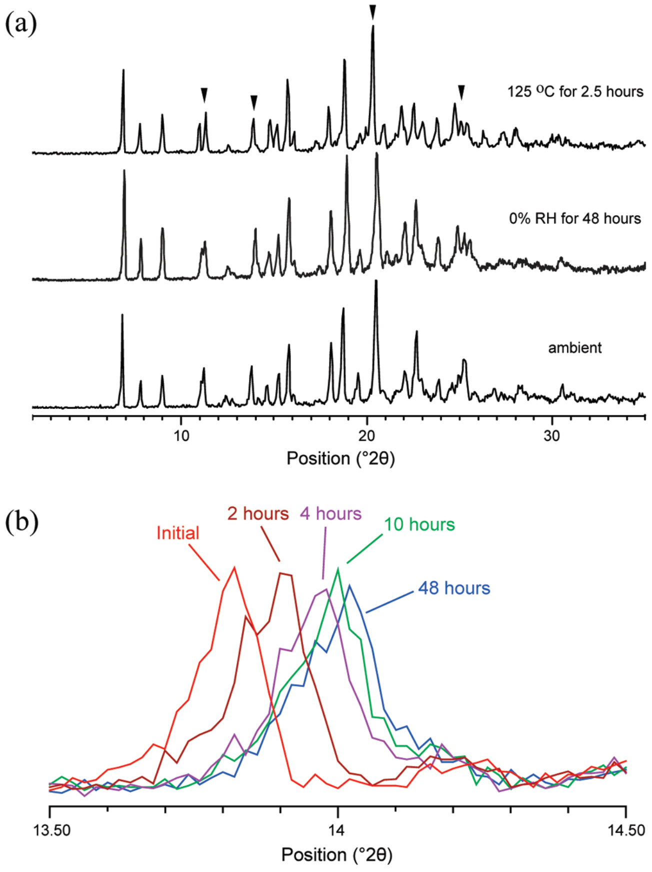

Figure 10. (a) Flat-plate PXRD patterns of **I** at ambient conditions, after 48 h at 0% RH at room temperature and after 2.5 h at 125 °C, with affected regions denoted by arrows. (b) PXRD patterns of **I** showing the reflection at ~14 deg 2θ as a function of drying time (under dry nitrogen) over a 48 h period at room temperature, highlighting the continuous nature of the dehydration process in powders.

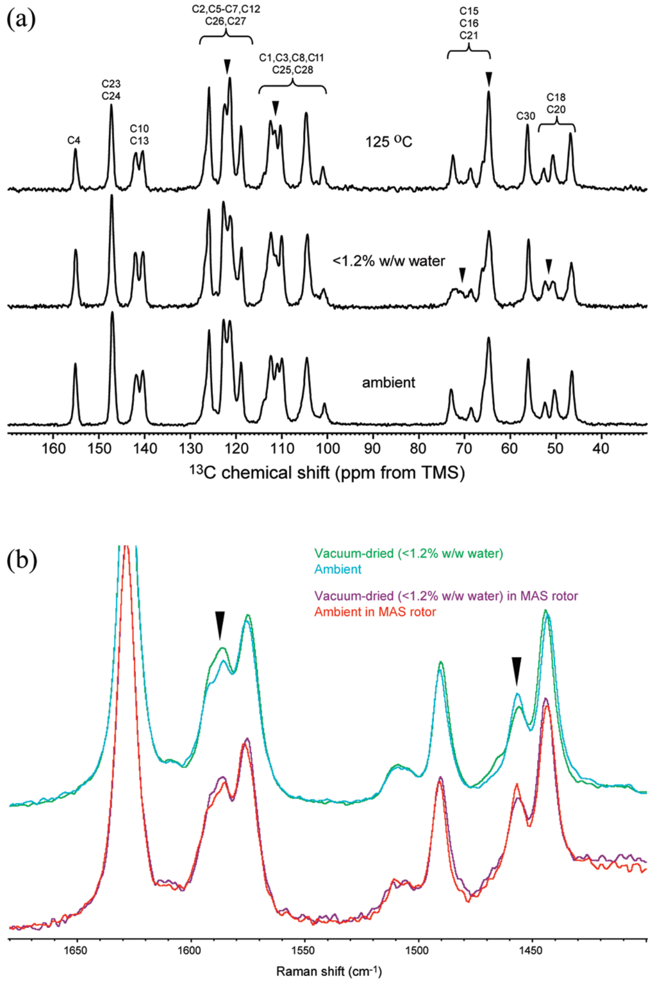

Figure 11. (a) ^{13}C CP-TOSS spectra of a sample of **I** at 125 °C and the vacuum-dried sample with 1.2% w/w water content compared to a spectrum of **I** stored under ambient conditions. Arrows denote changes observed in the spectra. (b) Expanded FT-Raman spectra of a dehydrated sample of **I** (vacuum-dried to < 1.2% w/w water) used for the SSNMR experiment compared to the same batch at ambient conditions, acquired with 2 cm^{-1} resolution. Two diagnostic bands for the dehydration process are noted with arrows. The off-scale band at 1628 cm^{-1} was used to normalize the spectra. Raman spectra of the same samples sealed within a zirconia MAS rotor are also shown, confirming the integrity of the samples. The zirconia rotor produces strong Raman signals at 643, 464, 320, 262, and 148 cm^{-1}, outside of this region (see Supporting Information).

change over a 0.4% w/w range. Above 80% RH, the change in slope seen in the GVS isotherm offers evidence of surface water uptake. The lack of hysteresis observed suggests that the dehydration is a reversible hydration state change, as phase changes usually exhibit hysteresis. An indistinguishable GVS isotherm was obtained for a sample of **I**-(*R*), with a similar critical RH of about 1% RH. DSC and TGA experiments on samples of **I** showed a relatively high final dehydration temperature of 125 °C. As seen in Figure 8a, DSC experiments detected a slightly higher peak dehydration temperature of **I**-(*R*) and **I**-(*S*) relative to **I** (100 °C versus 92 °C), providing evidence that water is more tightly held in the single enantiomer phases.

PXRD measurements on **I** were performed at elevated temperatures and a range of relative humidity settings, including the acquisition of patterns over several days as dry nitrogen was blown over the sample. No changes were detected in the PXRD pattern over a humidity range of 10%−90% RH. However, PXRD patterns obtained at 125 °C and at ambient temperature after two days of drying under nitrogen show a number of changes, which are depicted in Figure 10a. The similarity of the patterns suggests that only minor structural changes have occurred. Over the course of the two-day drying period, acquisition of PXRD patterns showed a continuous displacement of diffraction peaks to both higher and lower values of 2θ. An example of this is depicted in Figure 10b, where the change in the feature at approximately 14° 2θ is plotted with the drying time. A similar continuous shift in peak positions and shapes, including the feature at 14° 2θ, was also observed with increasing temperature up to 125 °C. The PXRD results thus indicate that the dehydration process in powders in **I** is continuous and devoid of any discrete transition.

The structural aspects of the continuous dehydration process were further investigated using FT-Raman and ^{13}C SSNMR spectroscopy. ^{13}C CP-TOSS spectra were collected at elevated temperature and low humidity. A vacuum-dried sample of **I** was quickly packed into a rotor in a low-humidity environment and analyzed. As shown in Figure 11a, only minor changes are observed in the spectra. The changes are confined to the regions assigned to carbons that are near to

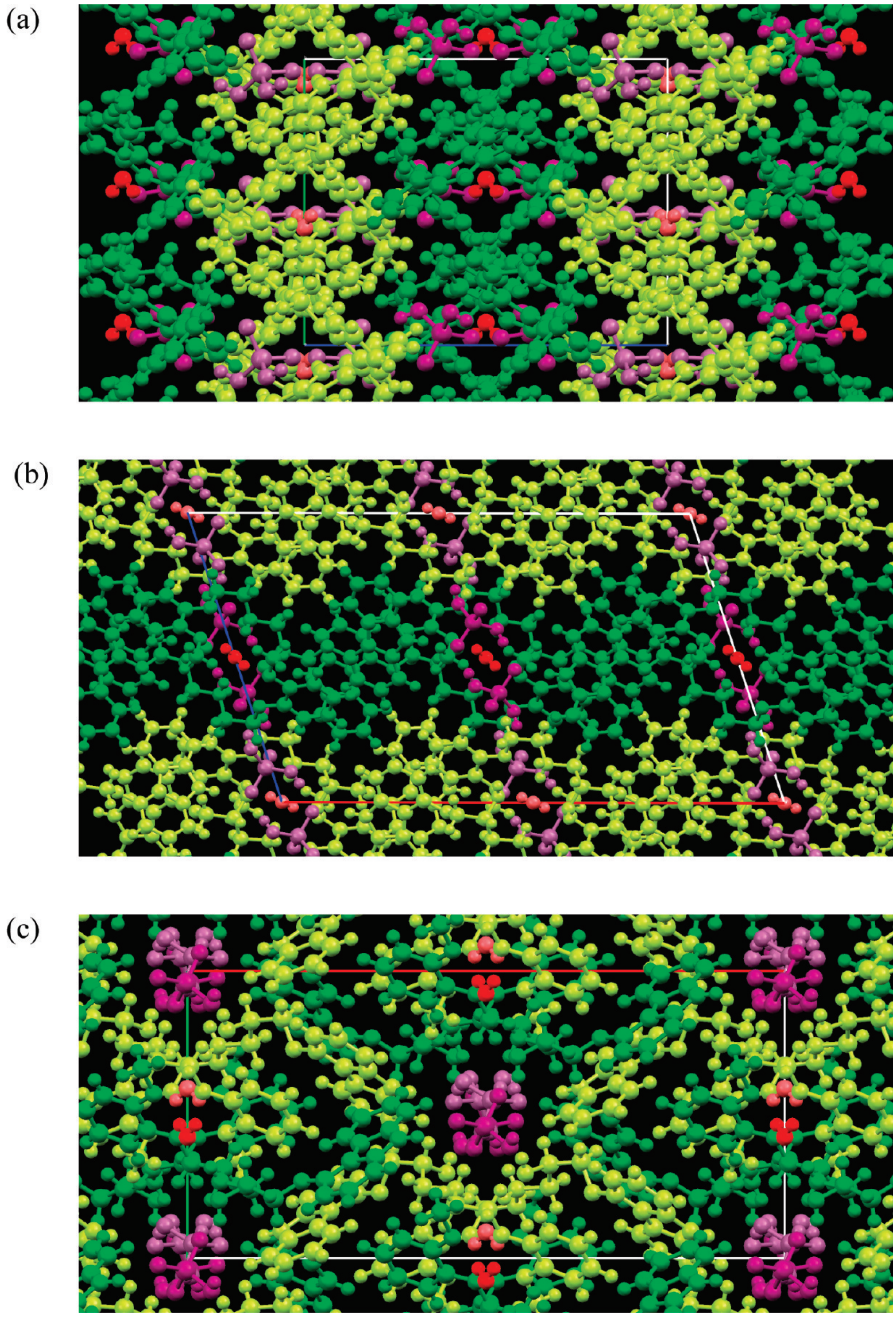

Figure 12. An illustration of molecular packing in the **I**-(*R*) crystal structure viewed in the direction of (a) the crystallographic *a*-axis, (b) the crystallographic *b*-axis, and (c) the crystallographic *c*-axis. The cations are colored green, the anions are purple, and the water molecules are red, with the darker and lighter of each color representing **A** and **B**, respectively. The disorder in the **B** cation has been omitted for clarity. Narrow channels are visible in the structure; the larger and more obvious of these run along the *b*- and *c*-axes (in the latter, the water molecules are in a staggered arrangement).

the water in the crystal structure of **I**. Only subtle changes are observed upon dehydration in the FT-Raman spectra in Figure 11b, in agreement with the SSNMR and PXRD results. FT-Raman spectra were also collected through the wall of the zirconia MAS rotors used to produce the SSNMR spectra in Figure 11a, confirming that the packing of the rotor had resulted in minimal rehydration. The combined SSNMR and Raman results thus indicate minimal changes to the molecular structure upon dehydration of the crystal structure.

Both the racemic and single-enantiomer crystal structures show water molecules contained in narrow tunnels running through the structure, as depicted for the crystal structure of **I**-(*R*) in Figure 12. The presence of tunnels suggests that the solvent can be removed without significantly disrupting the structure of **I**-(*R*). Extensive experience with channel hydrates has shown that the water can be both weakly or tightly bound and the lattice can either expand or not expand upon hydration or dehydration.[2,5−10] The size of the channels in Figure 12 combined with the relatively short water

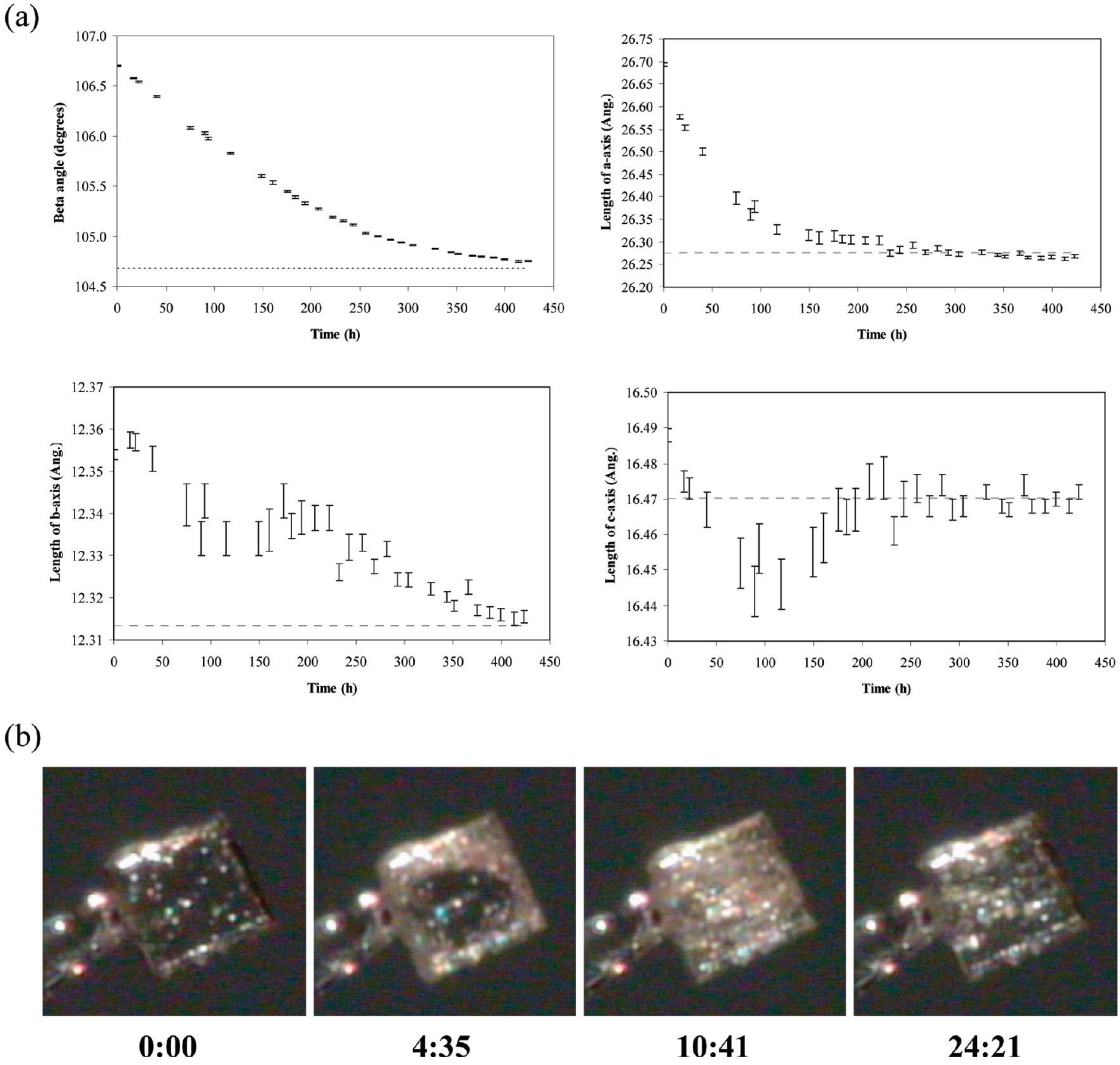

Figure 13. (a) Changes in unit cell dimensions during dehydration of a single crystal of **I**-(*R*) as measured by X-ray diffraction. Error bars are shown for each measurement. The dashed lines represent the value found upon returning to ambient conditions after heating and drying. (b) The change in appearance of the crystal of dehydrated **I**-(*R*) as it was rehydrated under ambient laboratory conditions. The time after the start of the rehydration is shown under each image as minutes:seconds. A video of the changes can be found in the Supporting Information.

hydrogen bonds immediately suggests that the water will not be easily removed, in agreement with a low critical RH and a high dehydration temperature from the GVS and TGA results.

SCXRD Studies of Dehydration. To obtain additional understanding of the dehydration effects seen in **I**, the single crystal of **I**-(*R*), originally flash-frozen to 90 K for the crystal structure analysis, was studied in situ on the diffractometer in a series of dehydration and rehydration experiments that lasted approximately seven weeks. Powders of **I**-(*R*) show DSC, TGA, and GVS results similar to those of **I** and thus the behavior of the high-quality crystal of **I**-(*R*) should be useful as a surrogate for **I**. The first dehydration was carried out at room temperature using the dry nitrogen gas stream over a period of 18 days. The unit cell dimensions of this crystal were monitored periodically. Although the water content of the crystal was not directly determined as part of the experiment, the results indicated that this process substantially dehydrated the crystal. The changes in the unit cell dimensions are plotted in Figure 13a. The most informative metric for following the dehydration was the β angle, which decreased by over two degrees. The change in the β angle with time was not linear, slowing throughout the dehydration. Changes in the other unit cell constants were less diagnostic. Rehydration of the dehydrated crystal was rapid under ambient laboratory conditions, completing in less than 30 min. The rehydration process could also be followed by changes in the single-crystal diffraction pattern occurring over this period (see Supporting Information).

The changes in β angle explain the results of the PXRD analysis at low humidity and high temperature, although the SCXRD study allows for a far more accurate determination of the trends in unit cell parameters than indexing and refinement of PXRD patterns. Pawley refinement of the PXRD patterns of dehydrated samples of **I** confirmed the same trend toward lower β angles for the racemic material upon drying. Interestingly, rehydration of the crystal of **I**-(*R*) could also be followed visually as shown in Figure 13b (see the Supporting Information for a time-lapse video of this process). The opaque areas seen during rehydration are believed to result from "fissures" created in the crystal, as β and the other unit cell dimensions rapidly change. The opaqueness starts at the outer boundaries of the crystal, moves through the whole crystal, and then clears from the edges, presumably as a result of a healing process within the crystal. On the basis of this visual evidence, the rehydration occurs via the smaller faces on the crystal and not through the main face. This corresponds to water entering the crystal in directions approximately perpendicular to the crystallographic *a*-axis (the main flat face of the crystal is the (001) face. In the view shown in Figure 13b, the *a*-axis of the unit cell is approximately perpendicular to the page, while the *b*-axis runs approximately parallel to the attached fiber. The opacity effect observed in the images is thus consistent with the narrow and tortuous channels observed in the packing plots in Figure 12, in that these views suggest water ingress and egress should occur perpendicular to the *a*-axis of the unit cell. Although 1D opacity effects are far more common,[55] a similar 2D opacity effect along the edges of a crystal has been reported for manganese(II) formate dihydrate.[2,56,57]

Throughout the single crystal study, it was found that the dehydration and rehydration processes were totally reversible, based on the unit cell constants determined before and after several cycles. Furthermore, heating the hydrated form to 373 K (100 °C) led to dehydration in less than 20 min without any clear visual signs of change to the crystal. The unit cell constants after the rapid dehydration were consistent with those obtained from the two-step process of dehydrating at 295 K (22 °C) and then heating to 373 K. This observation supports the presence of a single phase at 373 K, independent of the method of dehydration. After seven weeks of temperature and humidity changes, the crystal of **I**-(*R*) remained intact, with the only damage being superficial surface peeling and a minor crack.

Additional variable temperature studies on the dehydrated form suggested the presence of a constant phase between the temperatures of 166 and 328 K. At 166 K, a distinct but wholly reversible phase transition occurred. The low temperature unit cell appeared to be triclinic, suggesting 12 independent molecules in the asymmetric unit. This temperature region was not explored on powder samples (the lowest temperature reached on a powder sample was 173 K in the ^{2}H SSNMR study discussed in the next section). The low-temperature dehydrated phase of **I**-(*R*) was not investigated further; powders of **I** were studied by PXRD at liquid nitrogen boil-off temperatures (< 100 K) and did not show evidence of a similar transition under these conditions.

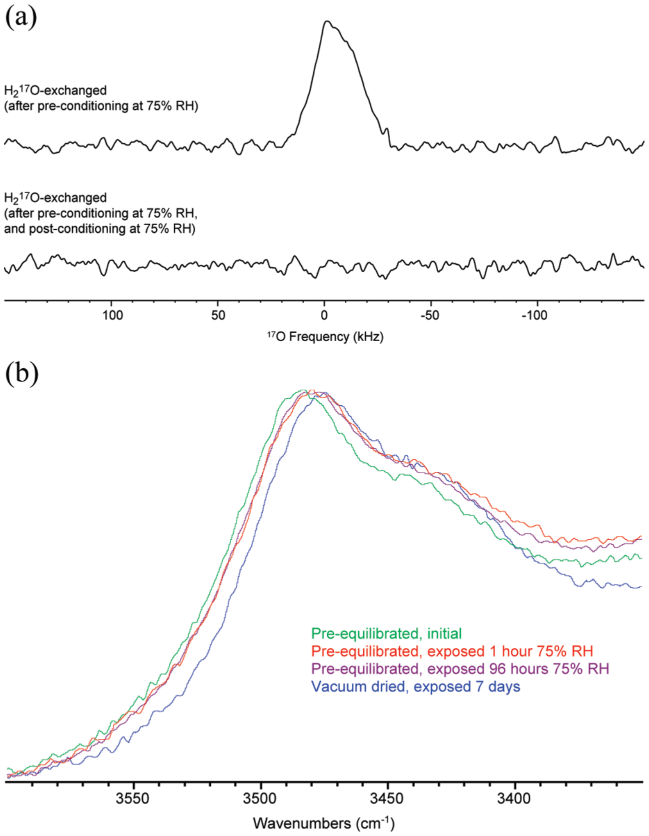

Figure 14. (a) ^{17}O static spin−echo SSNMR spectrum (obtained at 11.7 T and 273 K) of a sample exposed to 75% RH $H_2{}^{17}O$ (40% enriched) after preconditioning at 75% RH H_2O for 5 days. No signal is obtained after postconditioning this sample at 75% RH H_2O for another 5 days, illustrating the reversibility of this process. (b) IR spectra showing the OH stretching region of a sample exposed to 75% RH $H_2{}^{18}O$ (99% enriched) for different times after preconditioning at 75% RH H_2O for 5 days. The spectrum of a sample that was vacuum-dried prior to exposure to 75% RH $H_2{}^{18}O$ is shown for comparison. After 96 h, the material was re-exposed to 75% RH H_2O, and the IR band reverted back to its original position (not shown), confirming that water exchange is reversible.

Exchange with ^{2}H, ^{17}O, and ^{18}O-labeled Water and Analysis of Water Incorporation and Dynamics. Although the presence of tunnels in the lattice, the observed unit cell changes, and the optical changes potentially associated with fissures offer an explanation for the hydration behavior of **I**, exchange experiments were conducted with isotopically labeled water to gain a more detailed understanding of water exchange via SSNMR experiments and vibrational spectroscopy.[10,58,59] The ability of whole water molecules to exchange into the structure from the vapor phase was probed using $H_2{}^{17}O$ and $H_2{}^{18}O$. An exchange experiment was conducted on vacuum-dried **I** that was subsequently exposed to 75% RH $H_2{}^{17}O$ (40% enriched) for 5 days. The ^{17}O SSNMR spectrum of this sample, shown in Figure 14a, confirmed that whole water molecules may exchange under these conditions. A line shape with a 42 kHz width at its base, consistent with a second-order quadrupolar broadened interaction, is observed. The breadth of this signal is consistent with a C_q (quadrupolar coupling constant) of approximately 7−8 MHz, typical of a bound hydrate.[59−62] This second-order line shape is broadened and does not match the line shape expected from a single ordered oxygen site.[63] Because of the disorder in the SCXRD structure of **I** and broadening observed for the water signal in the ^{2}H MAS data (discussed below), attempts to obtain a more detailed fit of the ^{17}O line shape were not attempted. To follow the uptake of water dynamically, IR spectroscopy was employed. The ATR IR spectra as a function of exposure time to 75% RH $H_2{}^{18}O$ (99% enriched) are shown in Figure 14b, for a sample that was pre-equilibrated at 75% RH H_2O. The IR results show that ^{18}O-labeled water exchanges rapidly into the structure under these conditions. The peak maximum of the OH stretching vibration shifts by 6 cm^{-1} after 1 h of exposure and does not shift any further, as seen in comparison to the spectrum after 96 h of exposure. Subsequent re-exposure of the sample exposed to 75% RH $H_2{}^{18}O$ for 96 h to 75% RH H_2O led to a complete reversal of the shift in IR band position to its initial position, confirming the reversibility observed by ^{17}O SSNMR. The spectra in Figure 14b are compared to the spectrum of a sample that was vacuum-dried prior to exposure to 75% RH $H_2{}^{18}O$; the shift in the band maximum was 15 cm^{-1} for this sample, in agreement with the theoretical maximum for an asymmetric water stretching vibration based on reduced mass changes.

The IR results with and without preparatory vacuum drying suggest that the water exchange, although facile, cannot access the inside regions of the particles. The powder used in this study was composed of irregularly shaped plates with a median (X_{50}) particle diameter of 12 μm, and no evidence of unusually high porosity was observed as the specific surface area (SSA) was 1.8 m^2/g (measured by the Brunauer–Emmett–Teller adsorption method with nitrogen gas). Assuming a spherical particle, the surface area per particle would be approximately 450 μm^2, offering ample surface area for exchange. The evanescent wave in diamond ATR IR penetrates approximately 0.5 to 2 μm into the surface of a particle at 3500 cm^{-1}.[64] Thus, the partial exchange seen by comparing the 6 cm^{-1} shift to the 15 cm^{-1} shift is consistent with substantial exchange of water molecules in the outer regions of the particles. The vacuum drying procedure clearly enables access to deeper regions in the particles, consistent with the proposed fissures seen by optical and unit cell changes upon dehydration. This also helps explain the behavior of the GVS isotherm, in that minor changes in water content are observed from outer-surface effects until the critical RH is reached, at which point the exchange process is greatly enhanced.

Solid powders of **I** were also subjected to D_2O exchange, to study deuterium transport in the material and the presence of surface water. A sample of **I** was vacuum-dried and then exposed to 75% RH D_2O, while a second sample, pre-equilibrated at 75% RH H_2O, was also placed into the 75% RH D_2O chamber. The ^2H MAS SSNMR spectra of these two samples are indistinguishable as seen in Figure 15a, indicating that initial drying has no effect on the deuterium incorporation in **I**. Evidence of surface water is not seen in either spectrum but can be seen when additional exposure to 100% RH is performed as shown in Figure 15a by the appearance of a peak at ~5 ppm in the centerband. This confirms that the mass change in the GVS isotherm in the vicinity of 75% RH still involves bound water and not surface water.

The structural location of the deuteration in the crystal structure of **I** can be followed using several approaches. First, the multinuclear SSNMR spectra of the deuterium-exchanged sample were compared to that of the initial sample of **I**. Various minor changes in CP intensity (both increasing and decreasing peak intensities) were observed in a short contact time (1 ms) ^{13}C spectrum, while a 45% loss of CP intensity was seen in the short contact time (500 μs) ^{31}P spectrum of the deuterium-exchanged sample (see Supporting Information). Only a slight peak shift was observed for the N19 signal in the ^{15}N spectrum obtained with a 2 ms contact time, consistent with a distant isotope effect on hydrogen bonding but not direct exchange of the $NH_2{}^+$ protons. This confirms that no appreciable exchange has occurred at N9 or N19, while leaving open the possibility of exchange at O17, the oxygen atoms of the anion and the water molecule itself. Next, the ^1H spectra of the deuterium-exchanged sample were compared with the initial sample of **I**. A loss of intensity was observed for the peaks at 13.0 and 8.0 ppm (see Supporting Information). This corresponds to the appearance of intensity in the ^2H spectrum, as confirmed by the expanded plots of spinning sidebands in Figure 15a. On the basis of the observed chemical shifts, the deuterium exchange can be definitively linked to water, as confirmed by the ^{17}O SSNMR results and the P31 dihydrogen phosphate anion protons (via the ^1H and ^2H peak at 13.0 ppm and the slight intensity loss seen in the ^{31}P CP spectra). The presence of deuteration can be ruled out at N9 and N19, but deuteration at O17 cannot be ascertained from the SSNMR spectra.

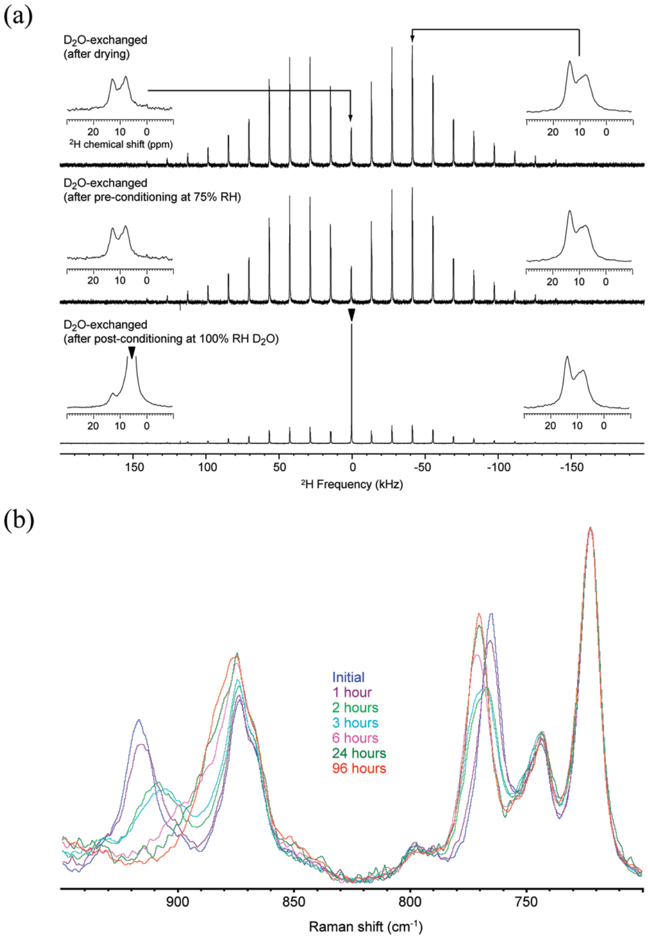

Figure 15. (a) ^2H MAS spectra (obtained at 9.4 T) of a sample of **I** stored at 75% RH D_2O for five days and after drying (insets show expansions of the centerband and +3 sideband). No evidence of surface water is observed (which can be distinguished in a sample exposed to 100% RH D_2O for 6 h by the observation of a peak at ~5 ppm in the centerband spectrum, denoted by arrows). (b) FT-Raman spectra (obtained at 2 cm^{-1} resolution) of **I** obtained from different exposure times to 75% RH D_2O after preconditioning at 75% RH H_2O for 5 days, showing the continuous nature of the deuterium exchange process over the course of several hours.

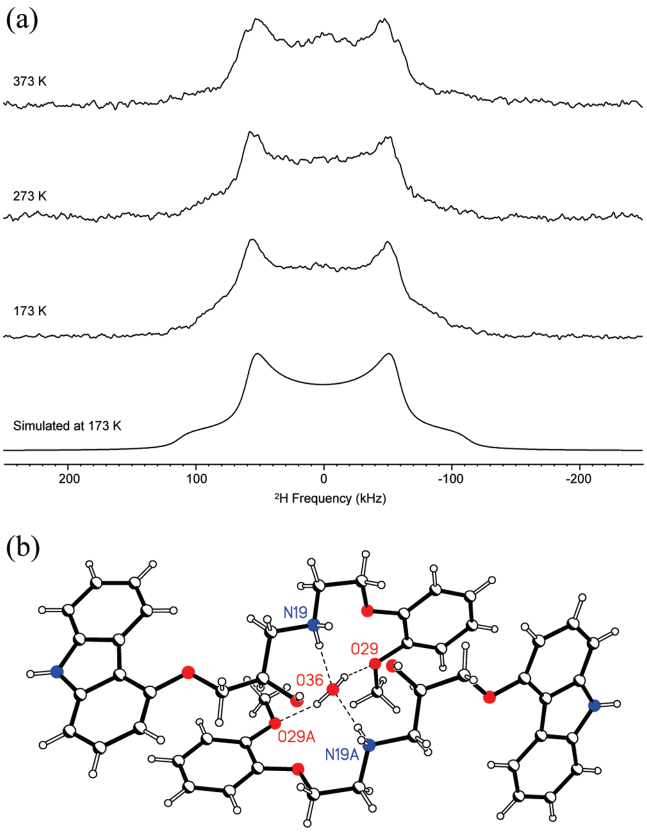

Figure 16. (a) Static ^{2}H NMR spectra (obtained at 9.4 T) of D_2O-exchanged **I** obtained over a 200 K temperature range. A simulated pattern is shown at the bottom, obtained by fitting against the 173 K experimental pattern, with $\nu_Q = 225$ kHz and $\eta = 0.0$. (b) The water environment of one of the water molecules from the crystal structure of **I**-(*R*). The water lies on a crystallographic 2-fold axis and engages in hydrogen bonds (dashed lines) to two symmetry equivalent cations, creating an unfavorable environment for jump motion. The environment of the second water molecule (not shown) is nearly identical but is instead hydrogen-bonded to two symmetry equivalents of the other independent cation.

The D_2O incorporation process was also followed dynamically using Raman spectroscopy. The results of exposure of two samples of the same powder used in the aforementioned SSNMR experiments are shown in Figure 15b. D_2O uptake is monitored by FT-Raman via the shifting of two bands in the spectrum, from initial values of 916 and 764 cm^{-1} to final values of 906 and 769 cm^{-1}. No evidence of an OD stretching vibration was observed in the Raman spectra of the final D_2O exchanged sample, most likely because this band was broadened by hydrogen bonding (a strong, broad band was observed in the IR spectra). The conversion was observed by FT-Raman to be complete after 5 days as evidenced by no further change in the spectra. The deuterium exchange process thus occurs on a slower time scale than exchange of whole water molecules, presumably because of limited motion inside the hydrated structure.

Since a large part of the ^{2}H signal can be ascribed to exchange of the half mole of water, the motion of the water molecules can be further investigated. Water is known to commonly execute jump motions (such as jumps about its C_2-axis and tetrahedral jumps) in a wide variety of inorganic and organic hydrate systems.[64,65] This type of dynamic behavior is readily observed by static ^{2}H SSNMR, which is also amenable to a wider temperature range than MAS methods.[10,59,65,66] Figure 16a shows the ^{2}H static spectra obtained over a 200 K temperature range. A simulated spectrum obtained by fitting the lowest temperature (173 K) pattern to a single-site deuterium line shape with $\nu_Q = 225$ kHz and $\eta = 0.0$ is also shown. The lack of a peak near to 0 kHz or any other changes indicates that there is no significant water motion over a 200 K temperature range, although there is evidence of a slight increase in intensity at 0 kHz at 373 K, indicating that motion may begin near the dehydration temperature. This lack of water motion is highly atypical given the normally facile jump motion of water in hydrates.[10,59,65,66] The hydrogen bonding network for the water molecule may be the cause of this; as shown in Figure 16b, the water strongly interacts with two donors and two acceptors.

Combining the IR, SSNMR, and SCXRD results, the dehydration, rehydration, and exchange processes in **I** and its enantiomers may be viewed as follows. Below the critical RH of ~1%, the material dehydrates by first losing moisture through surfaces perpendicular to the crystallographic *a*-axis, leading to unit cell changes and particularly a significant distortion of the β angle of nearly 2°. This results in optical opacity of the crystal, possibly from fissures created by the large change in unit cell parameters, which start at the surface, work through the crystal but ultimately disappear. The effect, a continuous disruptive process, is associated with improved access to deeper cells and more complete water exchange. No evidence was found of any major differences in the dehydration and rehydration process; they appear to be reversible images of one another. Significant exchange of whole water molecules occurs at the surface at 75% RH. There is no evidence that the 0.4% w/w change observed between 10 and 90% RH is due to surface water; hence it is likely that the water vapor activity leads directly to water exchange processes at the surface. A facile tunnel process is unlikely, as evidenced by the partial exchange obtained in the $H_2{}^{18}O$-exchange IR experiments and the narrow tunnels in the structure, but may contribute to the dehydration process, possibly across a limited number of unit cells. Although the fissure mechanism offers an explanation for the incorporation of water deep into the polycrystalline material, in combination with limited water ingress through the narrow tunnels seen in the packing diagrams of **I**, alternative possibilities do exist. Molecular motion could also provide a mechanism for rapid water incorporation without the presence of large channels, as was recently proposed for clarithromycin.[67] It is also possible that molecular motion allows for facile water incorporation at the particle surface and may be enhanced by the observed unit cell distortions under vacuum conditions, allowing for deeper water exchange.

From the bulk perspective, the hydration state behavior of **I** is similar to that of an isomorphic desolvate, with dehydration occurring as a continuous process in concert with significant structural adjustments. Among the isomorphic desolvates and channel hydrates published in the literature, we are not aware of an example with a critical RH as low as that of **I**.[5−10] The situation contrasts with that of typical isomorphic desolvates, where water easily moves along tunnels (potentially crossing many unit cells) to escape via a particular crystal face.[2,5−10,54,55] Despite its underlying structural complexity, powders of **I** behave in many respects like a tightly bound channel hydrate with a typical type I isotherm.

Conclusions

Racemic carvedilol phosphate (**I**) was found to exist as a solid solution of its enantiomers, which is a relatively infrequent occurrence in organic molecular crystals. Efforts to solve its crystal structure were hindered by weakly diffracting twinned crystals, from which data refinement was difficult. Multinuclear solid-state NMR analysis showed indications of disorder in the vicinity of the chiral center. Single enantiomer phosphate salts were therefore prepared and found to be isomorphic with the racemate using SSNMR and other techniques but lacking the disorder element detected in the SSNMR spectra of the racemate. A crystal of **I**-(*R*) did not exhibit twinning and yielded good diffraction data that were readily solved with an R_1 of $< 5\%$. The structure of the single enantiomer enabled a better understanding of the related racemic crystal structure. It is unusual for the single-enantiomer and racemic crystals of a compound to have such similar unit cell dimensions and crystallize as isomorphous phases, allowing for formation of a solid solution. That the racemate yields twinned crystals, whereas the enantiopure form does not even though the metric requirements for twinning are met, is also worthy of note. It may be possible that the development of twin domains in this system depends on the presence of both enantiomers; however, this cannot be confirmed at the present time. The increased disorder seen by SSNMR in **I** is associated with the formation of the solid solution, as confirmed by thermal analysis.

Both **I**-(*R*) and **I** were observed to be hemihydrates by SCXRD but can undergo isomorphic dehydration at low humidity and high temperature and take up additional water at higher humidity. The water is situated in narrow tunnels that run the length of the crystals. The dehydration and rehydration processes were found to be associated with a distortion of the unit cell, in turn leading to fissures that facilitate additional dehydration of the crystals or enhance molecular mobility. The critical RH of racemic **I** was found to be $< 1\%$ RH, which is extremely low in comparison to other known isomorphic desolvate systems. Exchange experiments with oxygen-labeled water were used to show that water molecules can appreciably exchange into bound positions in the lattice at ambient conditions and that enhanced exchange is obtained with preparatory vacuum drying. ^{2}H SSNMR experiments showed that the water molecules are unable to execute typical jump motions in the crystal lattice over a temperature range of 200 K, which is also unusual for a hydrate system and together with the narrow tunnel structure, offers an explanation for the low critical RH observed.

The use of complementary techniques in the study of this complex crystal system enabled both the solution of the racemic structure (the marketed form of this drug substance) and the understanding of the nature of disorder and water in the crystal, allowing for deeper insight into the structure than what would have been possible from the individual techniques. The results illustrate the benefits of applying a multidisciplinary approach to complex solid form science questions.

Acknowledgment. The authors thank Dr. Leo Hsu (GlaxoSmithKline) for performing the chiral preparative chromatographic separation of racemic carvedilol and Professor Judith Howard (University of Durham), in whose laboratories one of us (O.V.C.) prepared the crystals of **I**. The authors also thank Mr. Jerome Socha (GlaxoSmithKline) for assistance with water content determinations. Professor Gérard Coquerel (University of Rouen) and Dr. Ludovic Renou (Pharmorphix) are thanked for insightful discussions.

Supporting Information Available: A movie file illustrating the rehydration process for a single crystal of **I**-(*R*), crystallographic information files for the crystal structures of **I** and **I**-(*R*), and additional PXRD, NMR, and SSNMR data. This material is available free of charge via the Internet at http://pubs.acs.org.

References

(1) Bernstein, J. *Polymorphism in Molecular Crystals*; Oxford University Press: New York, 2002.
(2) Byrn, S. R.; Pfeiffer, R. R.; Stowell, J. G. *Solid-State Chemistry of Drugs*; SSCI: West Lafayette, IN, 1999.
(3) Lee, S. L.; Raw, A. S.; Yu, L. In *Drugs and the Pharmaceutical Sciences*; Informa Healthcare: New York, 2008; Vol. 178, pp 571−583.
(4) Eliel, E. L.; Wilen, S. H.; Mander, L. N. *Stereochemistry of Organic Compounds*; Wiley: New York, 1993.
(5) Morris, K. R.; Rodriguez-Hornedo, N. In *Encyclopedia of Pharmaceutical Technology*; Swarbrick, J.; Boylan, J. C.; Eds; Marcel Dekker: New York, 1993; Vol. 7, pp 393−440.
(6) Stephenson, G. A.; Groleau, E. G.; Kleeman, R. L.; Xu, W.; Rigsbee, D. R. *J. Pharm. Sci.* **1998**, *87*, 536–42.
(7) Khankari, R. K.; Law, D.; Grant, D. J. W. *Int. J. Pharm.* **1992**, *82*, 117–27.
(8) Stephenson, G. A.; Stowell, J. G.; Toma, P. H.; Xu, W.; Pfeiffer, R. R.; Byrn, S. R. *J. Pharm. Sci.* **1997**, *86*, 1239–44.
(9) Apperly, D. C.; Basford, P. A.; Dallman, C. I.; Harris, R. K.; Kinns, M.; Marshall, P. V.; Swanson, A. G. *J. Pharm. Sci.* **2005**, *94*, 516–23.
(10) Vogt, F. G.; Dell'Orco, P. C.; Diederich, A. M.; Su, Q.; Wood, J. L.; Zuber, G. E.; Katrincic, L. M.; Mueller, R. L.; Busby, D. J.; DeBrosse, C. W. *J. Pharm. Biomed. Anal.* **2006**, *40*, 1080–88.
(11) Tenero, D.; Boike, S.; Boyle, D.; Ilson, B.; Fesniak, H. F.; Brozena, S.; Jorkasky, D. *J. Clin. Pharmacol.* **2000**, *48*, 844–53.
(12) Stoschitzky, K.; Koshucharova, G.; Lercher, P.; Maier, R.; Sakotnik, A.; Klein, W.; Liebmann, P. M.; Lindner, W. *Chirality* **2001**, *13*, 342–46.
(13) Almeida, D. R. P.; Gasparro, D. M.; Pisterzi, L. F.; Torday, L. L.; Varro, A.; Papp, J. G.; Penke, B.; Csizmadia, I. G. *J. Phys. Chem A* **2003**, *107*, 5594–5610.
(14) Chilmonczyk, Z.; Ksycinska, H.; Aboul-Enein, H. Y.; Lee, W.-J. *J. Liq. Chromatogr. Relat. Technol.* **2001**, *24*, 2505–12.
(15) Lamprecht, G.; Gruber, L.; Stoschitzky, K.; Lindner, W. *Chromatographia* **2002**, *56*, S25–S29.
(16) In this work, isomorphs are defined as nearly identical crystal structures of materials that have different chemical compositions, including enantiomers and dehydrated forms. These types of situations are also referred to as isostructural forms in the literature. See Bernstein, J. *Polymorphism in Molecular Crystals*; Oxford University Press: New York, 2002; p 271; Kálmán, A.; Parkanyi, L.; Argay, G. *Acta Crystallogr.* **1993**, *B49*, 1039−1049. The definition of isomorphic desolvate used here and in ref 6 to describe desolvation with minimal structural changes is also consistent with this nomenclature.
(17) Datta, S.; Grant, D. J. W. *Nat. Rev. Drug Discovery* **2004**, *3*, 42–57.
(18) Mitchell, A. G. *J. Pharm. Pharm. Sci.* **1998**, *1*, 8–12.
(19) Brook, C. S.; Chen, W.; Dell'Orco, P. C.; Katrincic, L. M.; Louvet, A. M.; Oh, C. K.; Spoors, G. P. *PCT Int. Appl.* **2004**, WO 2004002419, 53 pp.
(20) Nyqvist, H. *Int. J. Pharm. Tech. Prod. Manuf.* **1983**, *4*, 47–48.
(21) Braun, S.; Kalinowski, H. O.; Berger, S. *150 and More Basic NMR Experiments*, 2nd ed.; New York: Wiley-VCH, 1998.
(22) Harris, R. K.; Becker, E. D.; Cabral de Menezes, S. M.; Goodfellow, R.; Granger, P. *Pure Appl. Chem.* **2001**, *73*, 1795–1818.
(23) Earl, W. L.; Vanderhart, D. L. *J. Magn. Reson.* **1982**, *48*, 35–54.
(24) Ratcliffe, C. I.; Ripmeester, J. A.; Tse, J. S. *Chem. Phys. Lett.* **1983**, *99*, 177–180.
(25) Metz, G.; Wu, X.; Smith, S. O. *J. Magn. Reson. A* **1994**, *110*, 219–227.
(26) Antzutkin, O. N. *Prog. NMR Spectros.* **1999**, *35*, 203–266.
(27) Fung, B. M.; Khitrin, A. K.; Ermolaev, K. *J. Magn. Reson.* **2000**, *142*, 97–101.

(28) Opella, S. J.; Frey, M. H. *J. Am. Chem. Soc.* **1979**, *101*, 5854–5856.

(29) Feike, M.; Demco, D. E.; Graf, R.; Gottwald, J.; Hafner, S.; Spiess, H. W. *J. Magn. Reson. A* **1996**, *122*, 214–221.

(30) Hohwy, M.; Jakobsen, H. J.; Eden, M.; Levitt, M. H.; Nielsen, N. C. *J. Chem. Phys.* **1998**, *108*, 2686–2694.

(31) van Rossum, B. J.; Förster, H.; de Groot, H. J. M. *J. Magn. Reson.* **1997**, *124*, 516–519.

(32) Lesage, A.; Sakellariou, D.; Steuernagel, S.; Emsley, L. *J. Am. Chem. Soc.* **1998**, *120*, 13194–13201.

(33) Zumbulyadis, N.; Antalek, B.; Windig, W.; Scaringe, R. P.; Lanzafame, A. M.; Blanton, T.; Helber, M. *J. Am. Chem. Soc.* **1999**, *121*, 11554–11557.

(34) Davis, J. H; Jeffrey, K. R.; Bloom, M.; Valic, M. I.; Higgs, T. P. *Chem. Phys. Lett.* **1976**, *42*, 390–394.

(35) The crystal structure data for **I**-(*R*) and racemic **I** have been deposited with the Cambridge Crystallographic Data Center under deposition numbers CCDC 775400 and 775401. This material can be obtained free of charge via www.ccdc.cam.ac.uk/data_request/cif, by emailing data_request@ccdc.cam.ac.uk, or by contacting the Cambridge Crystallographic Data Centre, 12, Union Road, Cambridge CB2 1EZ, UK; fax: +44 1223 336033.

(36) Pawley, G. S. *J. Appl. Crystallogr.* **1981**, *14*, 357–361.

(37) Herbst-Irmer, R.; Sheldrick, G. M. *Acta Crystallogr.* **1998**, *B54*, 443–449.

(38) Parsons, S. *Acta Crystallogr.* **2003**, *D59*, 1995–2003.

(39) Hunter, C. A.; Lawson, K. R.; Perkins, J.; Urch, C. J. *J. Chem. Soc., Perkin Trans.* **2001**, *2*, 651–669.

(40) Johnson, C. E.; Bovey, F. A. *J. Chem. Phys.* **1958**, *29*, 1012–1014.

(41) Brown, S. P.; Spiess, H. W. *Chem. Rev.* **2001**, *101*, 4125–4155.

(42) Vogt, F. G.; Katrincic, L. M.; Long, S. T.; Mueller, R. L.; Carlton, R. A.; Sun, Y. T.; Johnson, M. N.; Copley, R. C. B.; Light, M. E. *J. Pharm. Sci.* **2008**, *97*, 4756–4782.

(43) Vogt, F. G.; Clawson, J. S.; Strohmeier, M.; Edwards, A. J.; Pham, T. P.; Watson, S. A. *Cryst. Growth Des.* **2009**, *9*, 921–937.

(44) Schmidt auf der Gunne, J.; Eckert, H. *Chem.—Eur. J.* **1998**, *4*, 1762–1766.

(45) Coquerel, G. *Enantiomer* **2000**, *5*, 481–498.

(46) Huang, J.; Chen, S.; Guzei, I. A.; Yu, L. *J. Am. Chem. Soc.* **2006**, *128*, 11985–11992.

(47) Chion, B.; Lajzerowicz, J.; Bordeaux, D.; Collet, A.; Jacques, J. *J. Phys. Chem.* **1978**, *82*, 2682–2688.

(48) Renou, L.; Morelli, T.; Coste, S.; Petit, M.-N.; Berton, B.; Malandain, J.-J.; Coquerel, G. *Cryst. Growth Des.* **2007**, *7*, 1599–1607.

(49) Wermester, N.; Aubin, E.; Pauchet, M.; Coste, S.; Coquerel, G. *Tetrahedron: Asymmetry* **2007**, *18*, 821–831.

(50) Vogt, F. G.; Vena, J. A.; Chavda, M.; Clawson, J. S.; Strohmeier, M.; Barnett, M. E. *J. Mol. Struct.* **2009**, *932*, 16–30.

(51) Wallach, O. *Liebigs Ann. Chem.* **1895**, *286*, 90–143.

(52) Brock, C. P.; Schweizer, W. B.; Dunitz, J. D. *J. Am. Chem. Soc.* **1991**, *113*, 9811–9820.

(53) Jeffrey, G. A.; Yeon, Y. *Acta Crystallogr.* **1986**, *B42*, 410–413.

(54) Authelin, J. R. *Int. J. Pharm.* **2005**, *303*, 37–53.

(55) Perrier, P. R.; Byrn, S. R. *J. Org. Chem.* **1982**, *47*, 4671–4676.

(56) Eckhardt, R. C.; Flanagan, T. B. *Trans. Faraday Soc.* **1964**, *60*, 1289–1298.

(57) Clarke, T. A.; Thomas, J. M. *J. Chem. Soc.* **1969**, 2227–30.

(58) Ahlqvist, M. U. A.; Taylor, L. S. *Int. J. Pharm.* **2002**, *241*, 253–261.

(59) Vogt, F. G.; Brum, J.; Katrincic, L. M.; Flach, A.; Socha, J. M.; Goodman, R. M.; Haltiwanger, R. C. *Cryst. Growth Des.* **2006**, *6*, 2333–2354.

(60) Lemaitre, V; Smith, M. E.; Watts, A. *Solid State NMR* **2004**, *26*, 215–235.

(61) Zhang, Q. W.; Zhang, H. M.; Usha, M. G.; Wittebort, R. J. *Solid State NMR* **1996**, *7*, 147–154.

(62) Ueda, T.; Nakamura, N. *Z. Naturforsch.* **2000**, *55a*, 362–368.

(63) Butler, L. G. In *^{17}O NMR Spectroscopy in Organic Chemistry*; Boykin, D. W., Ed.; CRC Press: Boca Raton, FL, 1991; pp 2−17.

(64) Harrick, N. J. *Internal Reflection Spectroscopy*; Wiley: New York, 1967.

(65) Weiss, A.; Weiden, N. In *Advances in Nuclear Quadrupole Resonance*; Smith, J. A. S., Ed.; Heyden & Son Ltd.: London, UK, 1980; Vol. 4, pp 149−248.

(66) Barnes, R. G. In *Advances in Nuclear Quadrupole Resonance*; Smith, J. A. S., Ed.; Heyden & Son Ltd.: London, UK, 1974; Vol. 1, pp 335−355.

(67) Tian, J.; Thallapally, P. K.; Dalgarno, S. J.; Atwood, J. L. *J. Am. Chem. Soc.* **2009**, *131*, 13216–13217.